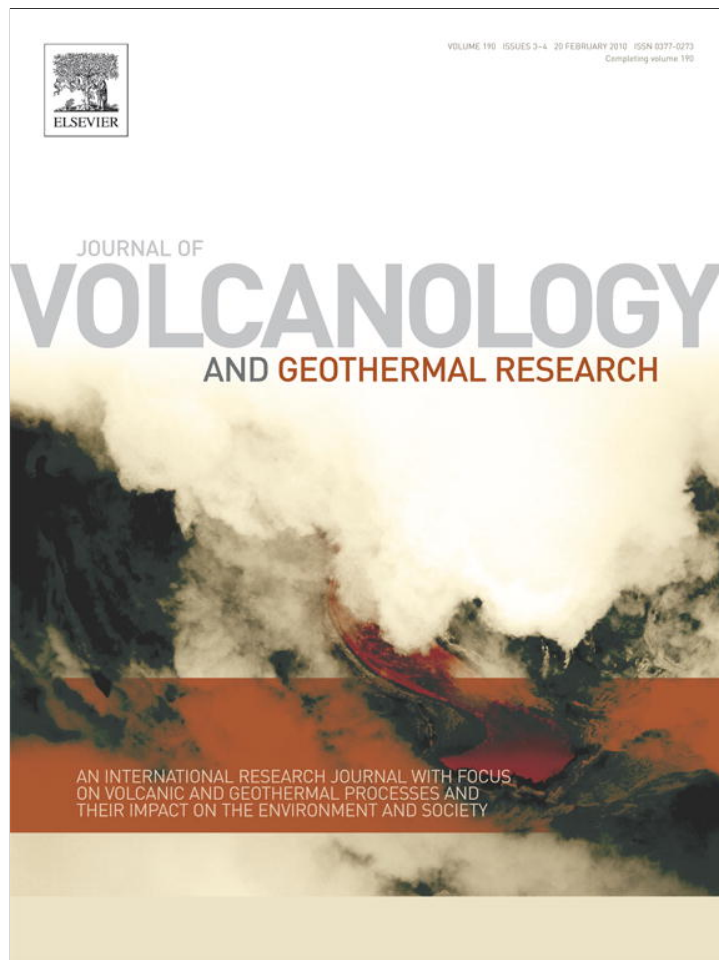


Provided for non-commercial research and education use.
Not for reproduction, distribution or commercial use.



This article appeared in a journal published by Elsevier. The attached copy is furnished to the author for internal non-commercial research and education use, including for instruction at the authors institution and sharing with colleagues.

Other uses, including reproduction and distribution, or selling or licensing copies, or posting to personal, institutional or third party websites are prohibited.

In most cases authors are permitted to post their version of the article (e.g. in Word or Tex form) to their personal website or institutional repository. Authors requiring further information regarding Elsevier's archiving and manuscript policies are encouraged to visit:

<http://www.elsevier.com/copyright>



Contents lists available at ScienceDirect

Journal of Volcanology and Geothermal Research

journal homepage: www.elsevier.com/locate/jvolgeores

Magma chamber stability in arc and continental crust

Leif Karlstrom^{a,*}, Josef Dufek^b, Michael Manga^a^a University of California at Berkeley, Berkeley, CA, USA^b Georgia Institute of Technology, Atlanta, GA, USA

ARTICLE INFO

Article history:

Received 10 February 2009

Accepted 5 October 2009

Available online 19 October 2009

Keywords:

magma chambers
volcanic plumbing
crustal rheology

ABSTRACT

The growth and thermo-mechanical stability of magma chambers in Earth's crust dictate the dynamics of volcanism at the surface, and the organization of volcanic plumbing at depth. We analyze a model of magma chamber evolution in which volumetric growth is governed by the mechanical focusing of rising dikes by the magma chamber, "magmatic lensing," as well as melting and assimilation of country rock. This modeling framework emphasizes the two-way coupling between chamber stresses and thermal evolution with specific compositions of intruding magma and country rock. We consider as end member compositional scenarios a "wet" environment magma chamber, in which basalt with 2 wt.% H₂O intrudes an amphibolitic country rock, and a "dry" chamber consisting of anhydrous basalt intruding tonalitic country rocks. Magma chambers that erupt, freeze, or reach dynamic equilibrium in the crust occupy distinct regions of a parameter space that measures the relative importance of depth, chamber pressurization, wall rock viscoelastic rheology, and thermal viability.

Lower crustal melt flux is the most important factor controlling chamber stability, but chamber depth and composition also help determine long-term dynamical behavior. In general, interactions between thermal and mechanical processes exert first-order control on chamber stability, defining four distinct regimes of magma chamber dynamics. In addition to thermally and mechanically unstable (freezing and eruptive) chambers, we find steady-state thermally viable chamber volumes are possible as well as a range of parameters for which chamber growth is roughly exponential in time and mechanically stable (no eruption occurs). Long-lived (>1 Ma) chambers generally result from lower crustal melt flux values that range from $\sim 10^{-4}$ to $\sim 10^{-1}$ m³/m²/yr for 20 and 40 km deep chambers and both compositional end members used in this study. However chambers become considerably less stable in cool shallow environments, particularly with anhydrous compositions of magma and country rock. Model predictions in this framework suggest that a range of observed intrusive structures in Earth's crust may be the result of magma chambers in different, clearly defined dynamical regimes.

© 2009 Elsevier B.V. All rights reserved.

1. Introduction

Magma transport within the crust is a fundamental and poorly constrained component of volcanism. It provides the only physical link between melting processes in the mantle and volcanic eruptions, and is responsible in large part for the assemblage of its own substrate — both oceanic and continental crust — through the emplacement and solidification of magma chambers, dikes, and sills. Crustal magma chambers are of particular importance in this transport system, as they form the largest-scale reservoirs that store rising melt, and modulate both the composition and dynamics of higher-level transport including volcanic eruptions. These structures reside at multiple levels of the crust and on large spatial scales: exposed calderas (e.g., Bachmann et al., 2007), plutons (e.g., Paterson et al.,

1995), layered mafic intrusions (e.g., Ernst and Buchan, 1997), as well as deeper structures inferred to be magmatic intrusions from remote imaging methods, such as lower crustal cumulate bodies (e.g., Cox, 1993). Yet it remains poorly understood where and how melt reservoirs are emplaced, what distinguishes one class of intrusion from another, and to what extent such intrusive igneous processes are linked to volcanism (Canon-Tapia and Walker, 2004). Many aspects of magma chamber growth and evolution subsequent to emplacement also remain controversial, especially in regards to the formation of large (10–100 km scale) intrusive structures.

Ultimately, what must dictate the longevity of a magma transport system is melt supply. However a variety of other factors may influence whether rising magma erupts to the surface, solidifies within the crust, or forms an active storage system as chambers. Rheological and material interfaces (such as the Moho or the brittle–ductile transition) provide a natural initial density trap for rising magmas (e.g., Kavanagh et al., 2006), and structural heterogeneities in the near surface may re-orient and capture dikes (e.g., Valentine and

* Corresponding author.

E-mail address: leif@berkeley.edu (L. Karlstrom).

Krogh, 2006). Large background deviatoric stresses will do the same – for example, extensional tectonic stresses can promote vertical dike transport without storage (Gudmundsson, 2006), while the presence of volcanic edifice loads or pressurized magma chambers tend to focus dikes subvertically, and may trap magmas (Pinel and Jaupart, 2003). Thermal viability is also important. Magma chambers and dikes in a long-lived transport system must survive the geothermal gradient, and thus transport enough enthalpy to remain liquid over long distances (Barboza and Bergantz, 2000; Rubin, 1995a).

It is also likely that many of the transport processes operating in the crust are strongly coupled to each other (Meriaux and Lister, 2002; Melnik and Sparks, 2005) and to the rheological evolution of the crust as whole (e.g., Dufek and Bergantz, 2005). In a previous paper (Karlstrom et al., 2009), we addressed some mechanical aspects of this coupling by modeling the focusing or “lensing” of dikes by a combined magma chamber and volcanic edifice system (Fig. 1). Here we extend this analysis to determine the thermal stability of such a system, focusing on the growth of initially small (~1 km) chambers. We model the time evolution of a magma chamber fed by a spatially and temporally stochastic distribution of rising dikes, and by doing so address:

1. Rheological and stress evolution associated with long-lived high melt fraction systems in a geothermal temperature gradient.
2. Average compositional evolution of the magma chamber and assimilation of country rock.
3. Stability of the system: will the magma chamber rupture, freeze, or exist in dynamic equilibrium within the crust for the lifetime of constant melt supply?
4. The possibility for large-scale growth of a high melt fraction reservoir.

This procedure aims to identify the key dynamical regimes to expect from dike-fed magma chambers in a viscoelastic crust. We map out a 3 parameter (initial volume, lower crustal melt flux, depth) magma chamber “stability field” for two end member emplacement scenarios – an arc setting where the country rock is amphibolite, and the intruding basalt is hydrous (2 wt.% H₂O), and continental crust composed of tonalite with intruding magmas of anhydrous basalt.

We find that the evolution of chamber volume and composition are strong functions of depth and composition, and generally that steady-state (“stable”) chamber volumes are more likely to exist for realistic lower crustal melt flux in hydrous environments. We also find a range of physical parameters for which chamber growth is roughly exponential in time and mechanically stable (i.e., no eruption occurs) that we refer to as “runaway”, suggesting that rapid large-scale growth of magma chambers is possible under some circumstances, provided that melt is continually supplied. While the details vary, stable or runaway chambers result from lower crustal melt flux values that range from ~10⁻⁴ to ~10⁻¹ m³/m²/yr for mid to lower crustal depths and both compositions in this study. Deeper and/or drier compositions produce a slightly broader range of runaway unstable chambers. The stability field results are then compared in a qualitative way to three classes of magmatic intrusions: caldera-forming shallow magma chambers, mid-crustal plutons, and layered mafic intrusions.

2. How to grow a large crustal magma chamber: Magmatic lensing

A magma chamber is commonly and loosely defined as a reservoir of high melt-fraction magma in the crust or upper mantle (possibly only transiently), that acts as a capacitor for magma ascent and as a place of chemical evolution through a combination of fractionation and melting (e.g., DePaolo, 1981; Marsh, 1989; Bachmann and

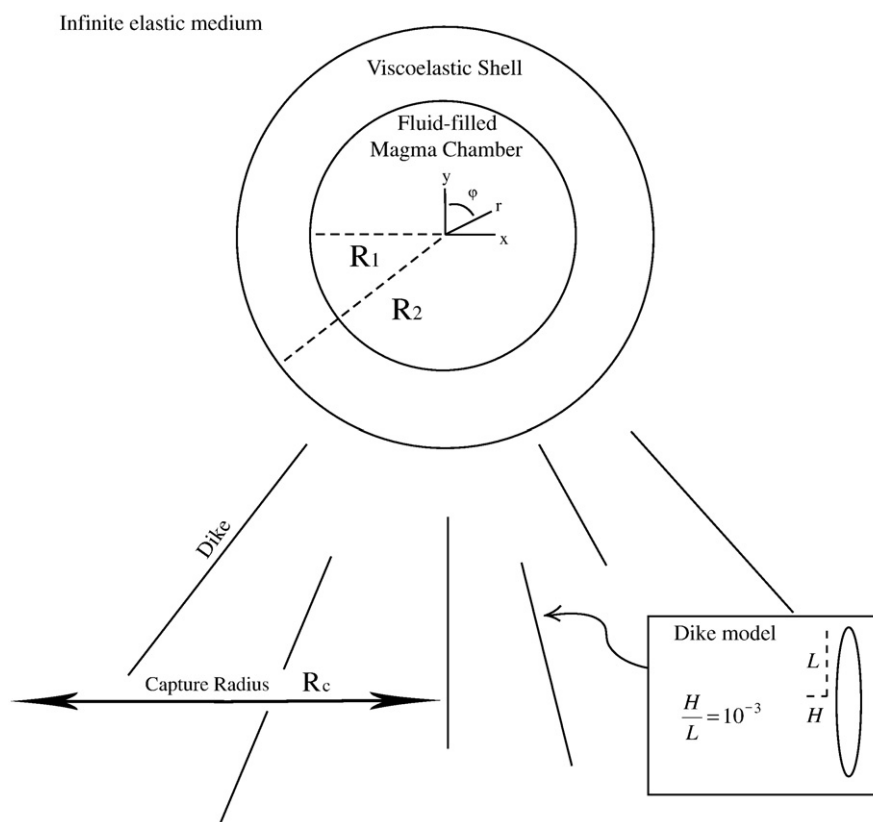


Fig. 1. The model problem, with a radial coordinate system centered on the cylindrical chamber. The magma chamber consists of a high melt fraction interior ($r \leq R_1$), and a viscoelastic shell ($R_1 \leq r \leq R_2$) that is overpressured and buoyant with respect to the surrounding elastic country rock. Dikes, modeled as uniformly pressurized ellipses with aspect ratio $h/l = 10^{-3}$, are focused toward the chamber from a region defined by the deviatoric stresses exerted by the chamber. This “capture radius” defines the magmatic lensing mechanism.

Bergantz, 2003). The mixture inside the chamber may become buoyant and/or over-pressured in time due to a variety of processes, including fractional crystallization, volatile exsolution and magma recharge, leading to deviatoric stresses in the country rock that may be tens of MPa in magnitude (e.g., Tait et al., 1989; Jellinek and DePaolo, 2003; Fowler and Spera, 2008). This stress field is geometry-dependent, and for all but the most symmetric chamber shapes (spheres), stresses at the chamber margin are concentrated in areas of high curvature (e.g., Sartoris et al., 1990; Gudmundsson, 2006; Grosfils, 2007). If the chamber overpressure is high enough, dikes will emanate from these locations of high deviatoric stress and transport magma from the chamber, thereby lowering the overpressure. This has been studied in a number of cases, for simple geometries (e.g., Meriaux and Lister, 2002; Pinel and Jaupart, 2005).

It is not well established how magma chambers are recharged, or whether melt in the lithospheric mantle and lower crust travels through diapirs (e.g., Miller and Paterson, 1999; Gerya et al., 2004), dikes (e.g., Clemens and Mawer, 1992), or in a network of channels (e.g., Spiegelman and Kenyon, 1992). Feeder dikes have been inferred to supply large mafic intrusions (e.g., Ernst and Buchan, 1997), lower crustal terrains (e.g., Williams et al., 2009), and must exist for thermally viable long distance transport (Bruce and Huppert, 1989). We assume here that dike transport is important, and that the propagation direction of rising melt should be broadly governed by the principle stresses in the surrounding medium, involving contributions from the rising magma itself and any background stresses (e.g., Muller et al., 2001). Dikes will propagate in a direction orthogonal to the least compressive principle stress in the medium at the dike tip. Therefore, magma chambers that are buoyant, over-pressured, or both may generate stresses that affect the trajectories of rising dikes by focusing, or “lensing,” dikes from a distance greater than the footprint of the chamber at depth – potentially many times the radius of the chamber for realistic overpressures (Karlstrom et al., 2009). Magmatic lensing is a mechanism by which magma chambers can attain the largest possible overpressures through recharge, although our model is consistent with any mechanism of unsteady magma supply.

3. A thermomechanical model

We develop a two-dimensional coupled thermal and mechanical model of dike focusing due to an over-pressured and buoyant cylindrical chamber with a viscoelastic shell (Fig. 1) in an otherwise infinite elastic medium to study the time evolution of a crustal magma plumbing system at different levels in the continental geotherm. The model contains a thermodynamic description of the chamber and its surroundings, a temperature- and time-dependent country rock rheology, and a mechanical model for chamber stresses based on the mechanism of magmatic lensing. Interactions between magma chamber and host rock are primarily responsible for determining the stability of the system. Emphasis is on simplicity in the model components; we do not strive for details of transport mechanics, focusing only on a few generally dominant processes. This approach seems a necessary first cut at a fully coupled crustal magma transport model.

Further simplification follows from a consideration of the important timescales involved in this process, summarized and quantified in Table 1. These are the magma supply timescale τ_d (the time for a dike to ascend from the source to the chamber), the Maxwell viscoelastic relaxation timescale τ_{ve} , the elastic pressurization timescale τ_e , and the timescale for thermal diffusion through the thickness of the viscoelastic shell τ_t . We assume that dike ascent speed V_{dike} is limited by the viscosity of the basaltic magma η_d , and subsequently find that dike ascent times are several orders of magnitude smaller than the others for timescales of interest (Table 1).

In evaluating the timescales above we assume two dimensional elliptical dikes of aspect ratio $H/L = 10^{-3}$ (Fig. 1) that propagate with a constant overpressure ΔP_d (see model description below for details).

Table 1

Important timescales for magma chamber – host rock interactions. Dike transit timescale measures ascent from source region to chamber, elastic timescale measures pressurization due to magmatic lensing of dikes through capture radius R_c , Viscoelastic timescale is the Maxwell relaxation time of the heated chamber wall rocks, and the Thermal diffusion timescale is measured over the typical thickness of the viscoelastic shell (10^2 – 10^3 m). Variables are defined in the text.

Name	Scaling	Range of times (s)
Dike transit timescale	$\tau_d \sim \frac{D\eta_d L}{\Delta P_d H^2}$	10^4 – 10^8
Elastic timescale	$\tau_e \sim \frac{\Delta P_{crit} V_c}{E Q_{avg} R_c}$	10^4 – 10^{12}
Viscoelastic timescale	$\tau_{ve} \sim \frac{\eta_{wr}}{E}$	10^8 – 10^{15}
Thermal diffusion timescale	$\tau_t \sim \frac{(R_2 - R_1)^2}{\kappa}$	10^{10} – 10^{12}

We take the viscosity of primitive basaltic melt $\eta_d = 10^2$ – 10^4 Pa s, dike transit length scales of $D = 10^4$ – 10^5 m, thermal diffusivity of $\kappa = 10^{-6}$ m²/s, the viscosity of wall rocks $\eta_{wr} = 10^{18}$ – 10^{25} Pa s, and Young's modulus E of wall rocks 10^{10} Pa. Chamber volume V_c and average melt flux Q_{avg} are taken in the range discussed in the Implementation section, R_c is the maximum capture radius of the magma chamber, and other geometric parameters are defined in Fig. 1.

Given these rough relations, we model the temporal evolution of the transport system in an iterative sequence of three one- and two-way coupled steps: 1) Dike propagation leading to mechanical chamber expansion, 2) Thermal evolution of the chamber and country rock 3) Viscous relaxation and rheological evolution around the chamber. The second and third steps of this process are two-way coupled. Though simplified, this model allows a rich variety of interactions (Fig. 2) that lead in time to chamber rupture, freezing or stable growth. In fact, consideration of Fig. 2 with respect to the timescales in Table 1 leads to a spectrum of model chamber dynamics (Results section).

3.1. The magma chamber

A magma chamber in the crust is modeled as an over-pressured and buoyant cylindrical inclusion surrounded by a viscoelastic shell and imbedded in an infinite elastic medium (Bonafede et al., 1986; Dragoni and Magnanensi, 1989). Our modeling takes place on a two dimensional slice of this system, making all volume estimates in this paper a function of the cylinder radius. The chamber grows through the addition of magma from dikes, and in some cases because of wall rock melting. Overpressure relative to lithostatic pressure in the chamber generates deviatoric stresses outside the chamber that decay with distance r as $\sim \Delta P/r^2 + \Delta \rho g/r$, where ΔP is the chamber overpressure, $\Delta \rho g$ is the magma buoyancy. Deviatoric stresses re-

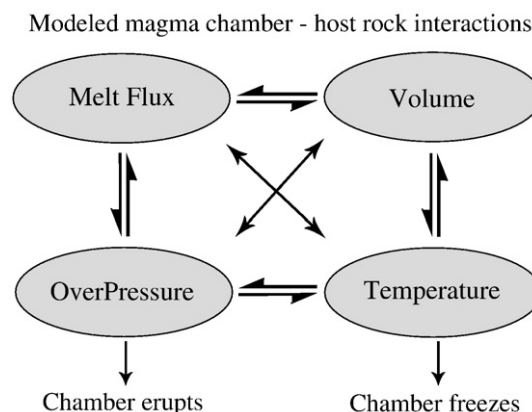


Fig. 2. Possible interactions in the coupled thermal and mechanical model. Feedbacks between melt influx, pressurization and phase change are responsible for the end member dynamical regimes: freezing and erupting chambers. Balance of these competing effects results in stable chambers.

orient rising dikes that travel within a region where these deviatoric stresses are large enough to affect dike propagation. We pick a simple model for dike propagation (discussed below) that results in dike focusing around the chamber where deviatoric stresses are ≥ 1 MPa (Karlstrom et al., 2009).

This region may be quantified at any depth below the chamber through the notion of a “capture radius,” measured from the center of the chamber at a given depth to the point where the magnitude of greatest deviatoric principle stress falls below 1 MPa (defined in Fig. 1). The capture radius will be zero at sufficient depth below the chamber, but may be several times the chamber radius at depths of 5–10 km below the chamber (Karlstrom et al., 2009). Rising magma will pass through the largest capture radius of the chamber on its way to the surface. Although this capture radius is geometry dependent, and is affected strongly by the presence of a free surface (e.g., Pollard, 1973; McTigue, 1987), capture by small or deep-seated magma chambers is well approximated by an infinite space solution (see Results section), and the far-field stresses calculated from a spherical chamber are similar to more complex geometrical formulations (e.g., Sartoris et al., 1990; Yun et al., 2006).

Geometric effects and material interfaces represent corrections to simple elastic cavity solutions in the appropriate limits, and are most pronounced in the near-field (where, incidentally, much of the interesting physics occurs). Our treatment of chamber stresses is not meant to capture all quantitative aspects of chamber rupture, and we retain an analytical approach to study a few clearly defined aspects of this problem, namely, the dynamic regimes that arise from a particular parameterization of chamber stresses and mechanical constitutive relations as well as free surface effects. A fully numerical treatment coupling advection, multicomponent magma thermodynamics and elasticity would be an interesting extension of this model, but is not attempted here.

In calculating the stresses in an infinite space, we apply the equilibrium equations of linear elasticity (Eq. (11)), with boundary conditions

$$\sigma_{rr,in}|_{r=R_1} = \Delta P + \Delta \rho g R_1 \cos \phi \quad (1)$$

$$\sigma_{r\phi,in}|_{r=R_1} = 0 \quad (2)$$

$$\sigma_{rr,in}|_{r=R_2} = \sigma_{rr,out}|_{r=R_2} \quad (3)$$

$$U_{r,in}|_{r=R_2} = U_{r,out}|_{r=R_2} \quad (4)$$

where σ_{in} and σ_{out} refer to stresses inside and outside the shell, U_{in} and U_{out} are displacements inside and outside the shell, ΔP is the chamber overpressure, $\Delta \rho g$ is the buoyancy of the magma chamber, R_1 , R_2 , and ϕ are defined in Fig. 1. Boundary conditions for the free surface case are slightly different, outlined in Appendix A. Our parameterization of gravitational body forces (Eq. (1)) provides a means of coupling thermally-induced buoyancy evolution in the chamber to stresses, and absorbs a reference buoyancy of the magma into the overpressure ΔP . Buoyancy is small compared to other sources of deviatoric stress in our model. We neglect the depth-dependent density of the crust, noting that density differences alone do not significantly affect the location of reservoir failure (Grosfils, 2007).

Viscoelastic solutions are then found via the correspondence principle (Fung, 1965), from which time-dependent stresses are found (Appendix A). These solutions have the property that deviatoric stresses in the viscoelastic shell decay in time at a rate determined by the shell viscosity (Fig. 3), although there are some differences between pressurized and buoyant chambers in this regard, as well as free surface effects (Appendix A). Viscous relaxation of chamber stresses may prevent chamber rupture, and is a possible mechanism for the growth of large over-pressured chambers (e.g., Jellinek and DePaolo, 2003). Viscoelastic relaxation of stresses affects rising dikes

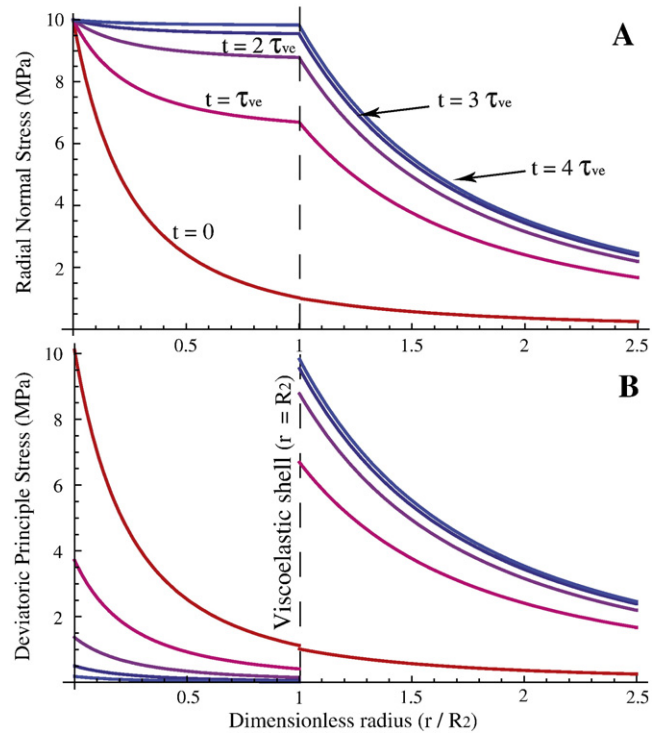


Fig. 3. A) Time evolution of the infinite space radial normal stress σ_{rr} (Appendix A) outside the magma chamber. The viscoelastic shell acts to propagate inner boundary conditions toward the edge of the shell in time. Curves are multiples of the Maxwell time of a chamber with shell viscosity of 10^{19} Pa s. B) Time evolution of greatest principle deviatoric stress outside the magma chamber. Deviatoric stresses inside the viscoelastic shell relax in time (but see Appendix A for differences between overpressure, buoyancy, and half-space solutions in this regard), while deviatoric stresses in the surrounding elastic medium increase.

as well, because the bulk crust is assumed elastic on dike-rise timescales, and dikes propagating in the country rocks ($r > R_2$) will still experience deviatoric chamber stresses (Fig. 3). Viscous creep effectively increases the chamber size by propagating elastic normal stress boundary conditions on the inner radius of the shell ($r = R_1$) to the outer radius ($r = R_2$) on the Maxwell timescale τ_{ve} (Appendix A).

The extent of the viscoelastic shell is determined through thermal considerations with a one-parameter melt fraction curve to relate crystal content of the magma to temperature (discussed below), and the viscosity is taken to be time and temperature dependent, but constant throughout the shell. This couples thermal evolution to mechanical effects. Thermal expansion of the magma and shell is neglected in the calculations leading to Eqs. (12)–(17), as the influence of thermal is roughly 6 orders of magnitude less than that of magma compressibility.

Not all chambers will exhibit a viscoelastic shell as formulated above, and indeed this is an important component of our model. Chambers that receive a sufficiently high melt flux through dikes will mechanically expand more rapidly than the thermal diffusion timescale, erupting before a shell forms. This condition requires that the Peclet number for chamber recharge (taken to be the ratio of chamber expansion from recharge and heat diffusion timescales in our model) must be larger than one:

$$Pe = \frac{Q_{avg} R_c R_1^2}{R_1^2 \kappa} = \frac{Q_{avg} R_c}{\kappa} > 1. \quad (5)$$

Under these conditions a magma chamber may quickly rupture to drain mass and overpressure. Because we are primarily interested in those magma chambers that drive surface eruptions, we assume that chamber draining occurs only when dikes propagate to the surface.

While certainly not strictly true in reality, as is evidenced by relic dikes and sills that terminated in the crust (e.g., Rubin, 1995b) and long-distance lateral transport through dikes (Ernst et al., 1995), this assumption simplifies the analysis.

We use a thermal criterion to determine the “critical” overpressure needed to drive dike propagation to the surface. By balancing the freezing and elastic opening of a crack, Rubin (1995a) and Jellinek and Depaolo (2003) derive the pressure required to propagate a dike from the source region to the surface. This pressure necessarily exceeds the tensile strength of rock, leading to chamber overpressures in our model that exceed the threshold dike propagation stress. We find values of this critical overpressure in the range of 20–100 MPa, consistent with magma chamber overpressures inferred from ground deformation measurements in volcanic areas (e.g., Newman et al., 2001; Yun et al., 2006), noting that inferences of magma chamber overpressure in shallow systems are sensitive to depth, and thus cannot be directly applied to rupturing of deep chambers.

Purely elastic formulations of reservoir failure that include tensile failure and gravitational loading in a self-consistent way (e.g., Grosfils, 2007) require rupture-inducing overpressures that exceed lithostatic in some cases. Conversely, chamber rupture based on laboratory tensile-failure experiments (e.g., Gudmundsson, 1988) implies dike overpressures that are too low to overcome the geotherm (Rubin, 1995b), and that reservoir failure may happen frequently. In place of a more complete failure model, we choose a constant “critical” overpressure of 75 MPa to rupture the magma chamber. This choice reflects uncertainty in the specific mechanisms of reservoir failure, which may involve different physics than we model here (e.g., Chen and Jin, 2006; Lengline et al., 2008). We expect that this value is an approximate upper bound on the chamber overpressure necessary to trigger an eruption, and models a (silicic) magma viscosity of 10^7 Pa s, surface heat gradient of 68 mW/m² (Rudnick et al., 1998), static Young's modulus E of 70 GPa, Latent heat L of 400 kJ/kg, heat capacity of 1100 J/kg K, and thermal diffusivity κ of 1 mm²/s. While different choices of these parameters will change the minimum critical overpressure needed for eruption, our main results are not sensitive to a particular choice.

3.2. Dike transport

Many quantitative dike models in the geologic literature are based on the assumptions of Linear Elastic Fracture Mechanics, and that dikes resemble fluid-filled pressurized and/or buoyantly driven opening-mode cracks (Rubin, 1995b). Cracks propagate when the potential energy released through propagation is sufficient to fracture rock at the crack tip (Griffith, 1920). This is a threshold energy criterion for propagation, and is a feature of all “critical” dike propagation models, though so-called “sub-critical” dike propagation (e.g., Atkinson and Meredith, 1987) is a viable magma transport mechanism over short distances (Chen and Jin, 2006). It is also possible that, in regions of partial melt, transport is dominated by porous flow and channelization (e.g., Spiegelman and Kenyon, 1992; Holtzman et al., 2003), though thermally viable long-distance transport is achieved through melt coalescence into a dike.

We model a dike as a uniformly pressurized ellipse of constant aspect ratio (Jaeger and Cook, 1969) in an infinite medium. In a polar coordinate system centered around the dike tip, taking ξ to be the radial coordinate and θ the angle from long axis of the dike, principle stress eigenvalues and (un-normalized) eigenvectors take the form

$$\sigma_{\text{dike}\pm} = \frac{K}{(2\xi)^{1/2}} [\cos(\theta/2) \pm 2 \sin(\theta)] \mathbf{v}_{\pm} \quad (6)$$

$$\mathbf{v}_{\pm} = \mathbf{e}_{\xi} + [\cos(3\theta/2) \pm \tan(3\theta/2)] \mathbf{e}_{\theta} \quad (7)$$

Here $\sigma_{\text{dike}\pm}$ are the magnitudes of principle stresses oriented along \mathbf{v}_{\pm} , \mathbf{e}_{ξ} and \mathbf{e}_{θ} are unit vectors centered on the dike tip, and K is the Stress Intensity Factor of a modified Griffith theory (e.g., Rubin, 1995b; Roper and Lister, 2005). Dikes propagate in this scheme if $K = \Delta P_d \sqrt{l} \geq K_c$, where K_c is the “critical” Stress Intensity Factor (Rubin, 1995b) and ΔP_d is the dike overpressure. We assume that dikes propagate with this minimum condition $K = K_c = 10^6$ Pa m^{1/2} at all times as a lower bound for continuous propagation (Karlstrom et al., 2009). Far-field deviatoric principle stresses in excess of dike stresses around the crack tip then reorient the trajectory of the rising dike. This dike model captures the physics of interest in the present application — (1) a dike will not propagate unless it is sufficiently driven (a threshold model), and (2) a dike exerts a stress field that helps to determine its own trajectory. We note that our approach to dike propagation in an external field is an approximation to the dynamics of truly coupled dike–chamber interactions, and may actually underestimate the efficacy of magmatic lensing (Meriaux and Lister, 2002). However, qualitative aspects of dike focusing are unchanged in more detailed studies. We exclude stress interactions between dikes, although such interactions can lead to interesting organization of magma transport (Ito and Martel, 2002; Kühn and Dahm, 2008). In the presence of large background stresses (such as the magma chamber considered here), dike interactions should be of lower order importance, although they may be important for the initial formation of magma reservoirs (Kühn and Dahm, 2008). We also note that while dikes are emplaced elastically, this does not mean that their surroundings (particularly the magma chamber and wall rocks) are strictly elastic. Hence, dike interactions and chamber evolution may occur over different timescales (Table 1).

While magma supply to the lower crust is not certain, a variety of studies have generally found lower bounds on the order of 10^{-3} m³/m²/yr to 10^{-4} m³/m²/yr in arc settings (see (Dufek and Bergantz, 2005) for a compilation of this data). We use the stochastic framework of Dufek and Bergantz (2005) to model continued melt supply through dikes. Dikes are intruded randomly in space and in time at the base of our simulated domain, constrained only to conform to a long-term average volume flux. We use a Monte Carlo algorithm (Manno, 1999) to produce a spatially random distribution of dikes with a Gaussian distribution of melt volume (and therefore size). These dikes propagate vertically unless far-field deviatoric stresses exceed stresses near the dike tip, at which point dike trajectories are re-oriented to follow the least compressive principle stress.

3.3. Thermochemical model

Much effort has been devoted to understanding the thermal evolution of magma chambers. While complex multi-component convective processes may occur throughout the lifetime of the chamber (e.g., Turner and Campbell, 1986; Ruprecht et al., 2008), the enormous crustal thermal resistor ensures that conduction will be the primary mode of heat transfer near the wall of a magma chamber, driven both by the sensible and latent heat content of the magma chamber. The rate-limiting factor in both cooling/crystallization and possible heating/melting events is therefore conductive heat transfer between the chamber interior and the host rock (Carrigan, 1988; Marsh, 1989).

While simple analytic conductive cooling models have been used widely to investigate the thermal evolution of magma bodies (e.g., Younker and Vogel, 1976; Spera, 1980; Hort, 1997; de Silva and Gosnold, 2007), models that take into account laboratory melt crystallization experimental results (e.g., Annen and Sparks, 2002; Dufek and Bergantz, 2005) and multi-component heat transfer (e.g., Spera and Bohron, 2001; Gerya et al., 2004) allow for more detailed petrologic predictions. We use a nonlinear melt fraction–temperature curve as a proxy for composition in two end-member cases: country rock of amphibolite (Dufek and Bergantz, 2005) or tonalite (Petcovic and Dufek, 2005) bulk composition, and intruding basalt that is either anhydrous or contains 2 wt.% H₂O (Appendix B). Evolution of melt

fraction can then be used as a proxy for compositional evolution of a magma chamber, including chamber buoyancy and the mixing of melt from country rock and dikes.

We use an Alternating Directions Implicit (ADI) finite difference numerical scheme to solve the time-dependent heat conduction problem based on the treatment of Dufek and Bergantz (2005), but modified to include a more general local enthalpy to couple a mechanical model to the thermal model. Conservation of energy for the system dictates:

$$\frac{\partial H(\mathbf{x}, t)}{\partial t} = \frac{\partial}{\partial \mathbf{x}} k_{\text{mix}} \left(\frac{\partial}{\partial \mathbf{x}} T(\mathbf{x}, t) \right) \quad (8)$$

where $H(\mathbf{x}, t)$ is the local enthalpy at point (\mathbf{x}, t) , given by

$$H(\mathbf{x}, t) = \rho_{\text{mix}} \int_{T_{\text{ref}}}^{T(\mathbf{x}, t)} c_{\text{mix}} dT + \rho_{\text{mix}} f(\mathbf{x}, t) L + P \delta V(\mathbf{x}, t). \quad (9)$$

We use enthalpy to parameterize local energy, because it remains a continuous function through phase changes. \mathbf{x} is the position vector of the local energy balance, t is time, $L = 400 \text{ J/kg}$ is the latent heat of fusion, and $T(\mathbf{x}, t)$ is temperature. The variables k_{mix} , c_{mix} and ρ_{mix} refer to mixture quantities, defined in Appendix B, that allow us to treat mixing and melting of the country rock in the magma chamber. The work term $P \delta V(\mathbf{x}, t)$ is a local quantity that reflects the addition of new magma to the chamber due to dike lensing, and $f(\mathbf{x}, t) \in [0, 1]$ is the local melt fraction. We impose a steady state geothermal gradient upon the country rock with a surface heat flux of 68 mW/m^2 and a surface temperature of $10 \text{ }^\circ\text{C}$, using reflecting temperature boundary conditions on the sides of the 2D numerical domain. More details about the specifics of this thermal model can be found in Dufek and Bergantz (2005), although we assume here that dike transit does not significantly affect the background geotherm, because of the difference in timescales (Table 1).

The crystal content of a magma has a profound impact on its rheology (e.g., Marsh, 1981), and we use melt fraction as a proxy for purely viscous, visco-elastic or elastic behavior in the mechanical model. Regions that contain 0.6 or higher melt fraction (Eqs. (58)–(62)) are considered purely viscous (radius $r < R_1$ in Fig. 1), and regions with 0.05 melt fraction or lower are considered purely elastic ($r > R_2$). Melt fractions between 0.05 and 0.6 ($R_1 < r < R_2$) are modeled with a Maxwell viscoelastic rheology, with an exponential temperature dependent viscosity (Appendix B). Viscosities calculated in this way are a crude approximation to more detailed parameterizations of magma viscosity based on dissolved water content, crystallinity and silica content (e.g., Scaillet et al., 1998; Hui and Zhang, 2007).

3.4. Important model approximations

Studies of magma chamber convection have shown that mixing processes, may have important consequences for the rejuvenation and eruptibility of large silicic systems (Bachmann and Bergantz, 2003), as well as cooling and crystallization rates (e.g., Hort, 1998). External eruptive triggering (e.g., Roche and Druitt, 2001) or volatile exsolution in shallow chambers may have similar first order effects (e.g., Tait et al., 1989; Huppert and Woods, 2002). However, these processes are not within the scope of this work. Here we exclude explicit dynamics within and around the magma chamber, and assume that the interior is well mixed at all times.

By excluding advection in our simulations, we also assume that lower crustal rheology is elastic on the timescales of magma chamber evolution, with the diapiric rise of a large buoyant magma chamber within the crust being negligible on the timescale of magmatic lensing. This assumption is readily justified both observationally and theoretically. The Stokes rise-velocity for a magma chamber scales as $\rho g R^2 / \mu \sim 10^{-10} - 10^{-12} \text{ m/s}$, much slower than typical dike speeds, and abundant field evidence for diking in lower crustal terrains (e.g.,

Dumond et al., 2007) demonstrates that the mid to lower crust is elastic on sufficiently short timescales.

We use an analytic solution to determine viscoelastic stresses and a numerical solution for thermal evolution, so there are a number of approximations necessary to make the thermal and mechanical calculations consistent. While the analytical solution limits the extent to which the chamber can respond to an anisotropic thermo-mechanical environment, this approximation significantly simplifies the calculations and reduces the parameter space that must be explored. It allows us to focus on the dynamic behavior that results from interaction between heat diffusion, viscoelastic relaxation and elastic pressurization in a relatively simple system. The evolution of damage due to repeated diking is neglected, although it is almost certainly an important component of magma transport (especially in the shallow crust), as propagating dikes will be influenced by structural heterogeneities (Gaffney et al., 2007). To maintain a circular magma chamber that thermally evolves in a vertical temperature gradient, we impose circular symmetry on the magma chamber by organizing the entire melted region after each time step into 7 circular rings of constant melt fraction. The innermost ring is completely liquid ($f(\mathbf{x}, t) = 1.0$), the next has $f(\mathbf{x}, t) = 0.8$, and so on. For rings that are below the critical melt fraction of 0.6 (viscoelastic rheology), we use the highest ring temperature to determine the viscosity of the entire shell. This choice does optimize the viscoelastic relaxation effects, and thus represents a lower bound for the shell viscosity. Particular choices of melt fraction curve (Appendix B) result in shell viscosities of $\sim 10^{19} - 10^{22} \text{ Pa s}$ for both tonalite and amphibolite. The re-organization of melt in this way is a crude approximation for mixing processes inside the chamber, and is consistent with the dynamical assumption that the chamber interior is well mixed at all times.

Differences in the petrology of amphibolite and tonalite require that we treat the melting of these country rocks in different ways. Amphibolite is a mafic end-member proxy for lower crustal composition in arc settings, and its major element composition is similar to basalt (e.g., Helz, 1982; Wolf and Wyllie, 1994). We therefore treat the melting and solidification of basalt and amphibolite country rocks interchangeably, by assimilating melted country rock into the chamber melt at each time step. This is consistent with the assumption of a mixed chamber, and ensures a stable solution. The more evolved nature of amphibolitic partial melts is not accounted for, as it should constitute a negligible perturbation to the bulk chamber composition.

Tonalite, however, is chemically dissimilar to basalt, being essentially in the second stage of its petrological evolution (Wolf and Wyllie, 1994). As such, we treat the melting of tonalite country rocks with two separate binning procedures for basaltic and tonalitic melt, with tonalitic melt always placed outside the intruded basalt. Because tonalite has a lower melting temperature than the anhydrous basaltic input, this can result in a “jelly sandwich” configuration, where partially solidified basaltic material is sandwiched between high melt fraction tonalite and basalt. We choose the inner melt rings (basaltic composition) to determine the extent of the viscoelastic shell. This procedure does not treat the mixing processes that must occur between these two magmas, but our conclusions should depend more on a consistent treatment of melting than on detailed advective dynamics.

Finally, while we use the mechanism of magmatic lensing to model chamber recharge, subsequent thermal evolution is consistent with other means of unsteady magma supply through dikes. While details will vary, the main dynamic regimes that we find depend primarily on the average supply of enthalpy to the chamber, not the specifics of the magma delivery system.

4. Implementation

We implement the magmatic system model in three steps, capturing an averaged thermomechanical coupling between components of the plumbing system.

4.1. Step 1. Magmatic lensing

We use a dynamic model of dike propagation in which a stochastic distribution of dikes, with (2D) volumes that satisfy the mean lower crustal melt flux at the base of a discretized rectangular domain, rise toward a magma chamber. Dikes propagate incrementally; if the chamber stress field at a grid point is greater than the dike-tip stress field, we re-orient the dike along the greatest principle stress eigenvector. Otherwise, the dike moves vertically. We use the infinite space solutions (Eqs. (12)–(17)) to calculate the stresses for simulations at 20 and 40 km depth, assessing the free surface effects separately.

If a dike intersects the magma chamber, the chamber volume increases according to $V_{\text{new}} = V_{\text{old}} + V_{\text{dike}}$, and chamber overpressure according to the thermodynamic condition $P_{\text{new}} = P_{\text{old}} + \beta^{-1}(V_{\text{new}} - V_{\text{old}})V_{\text{old}}^{-1} + \delta P_{\text{pc}}$. This assumes that pressure changes propagate throughout the chamber very rapidly, so that local phase changes contribute to the entire chamber pressure. Magma compressibility β is calculated assuming a basaltic composition (Dobran, 2001), and thermal expansivity is neglected. Pressures induced by phase change δP_{pc} (determined by the thermal calculation) are included. We assume that, as an upper bound, there is a 15% volume change due to melting or solidification of magma (Dobran, 2001). Although this volume change varies with mineral phase (Ghiorso and Carmichael, 1987), most important phases (with the exception of plagioclase) exhibit a negative volume change upon solidification, and we assume that holds for the bulk magma here. The liquid interior of the chamber is assumed to have a basaltic dike composition initially, but we track chamber bulk compositional evolution through the mixture quantities (Eqs. (64)–(66)). Dike propagation continues until all dikes either reach the chamber or the top of the numerical domain. If a dike intersects another dike, dike volumes are additive.

4.2. Step 2. Thermal evolution

Using the updated chamber volume (and heat content) from the dike, we discretize melt into rings of constant melt fraction (7 total for amphibolite/hydrous basalt, and 14 total for tonalite/anhydrous basalt). We next implement the ADI scheme to determine the new temperature field solving Eq. (8), using local differences in melt fraction to update the latent heat. The work term added to Eq. (9) is assumed constant over the volume of the chamber at each time step. We iterate until convergence is achieved, then update melt fraction according to Eqs. (58)–(62), and calculate inner and outer chamber radii. If the outer radius reaches the boundary of the domain, the simulation is stopped. These cases are then run with a larger domain, however, there are parameters under which chamber growth exceeds all domain sizes tested (see Results).

4.3. Step 3. Viscoelastic relaxation

With the inner and outer radii determined by the thermal calculation, we first check for either 1) possible chamber eruption due to excess of deviatoric stress at anywhere within the viscoelastic shell, i.e. $\sigma_{\text{rr, in}} - \sigma_{\phi\phi, \text{in}} > \Delta P_{\text{crit}}$ (Jellinek and DePaolo, 2003), or 2) chamber freeze-out $R_1 \leq 2$ grid cells (where $R_1 \leq 60$ –150 m, depending on the chamber size). If either occurs, the simulation is stopped. If not, we calculate new stresses throughout the domain according to Eqs. (12)–(17), with time step $t = 500$ years (a step size consistent with long-term averaged melt supply). In these calculations, the constant shell viscosity is updated to match the highest temperature in the shell, and we check that other choices (for example the average shell temperature) do not significantly affect the results.

This sequence is repeated for 2000 time steps (1 million years), or until eruption/freezing occurs. The model as formulated contains five variable parameters: Lower-crustal melt flux, initial chamber radius ($R_1 = R_2$), initial chamber overpressure (ΔP), bulk composition of the

dike and country rock (Eqs. (58)–(62)), and depth below the surface. However, because of the coupling between thermally and mechanically determined overpressure, choice of the initial ΔP is somewhat arbitrary, as both pressure and buoyancy are determined at each time step to ensure consistency between thermal and mechanical models. ΔP is set to an initial value of 10^6 Pa in all runs.

We run simulations with 8 choices of averaged lower crustal melt flux ($Q_{\text{avg}} = 10^{-5}$ m³/m²/yr– 10^0 m³/m²/yr). This range encompasses observed estimates of lower crustal melt flux in arcs (Dimalanta et al., 2002), as well as the higher values estimated from decompression melting mantle plume models (Olson, 1994; Farnetani and Richards, 1995). We use 4 values of initial radii (100, 500, 1000 and 2500 m), and 2 chamber depths (20 and 40 km) to test the effect of mid to lower crustal temperature profiles on chamber stability. A more thorough test of chamber depth using a halfspace viscoelastic solution (Eqs. (41)–(46)) is also performed for a few cases to ensure that neglect of the free surface does not affect results, and to test the depth dependence of dynamic chamber stability. However, shallow chambers are not the main focus of this study. We also test 2 end member compositional scenarios. Amphibolite composition country rocks are used as a proxy for arc environments, and are also similar to expected lower crust compositions (e.g., Christensen and Mooney, 1995). We do 32 runs at 20 km and 40 km depth for amphibolite. Tonalite composition country rocks are to be expected in more compositionally evolved settings. Because rocks of this composition partially melt at lower crustal depths, we do 32 runs at 20 km depth only. The total number of simulations is thus 96. Repeat simulations were undertaken in all cases where the stochastic distribution of dikes seemed to affect results. However, in most cases the results are robust to multiple runs. Resolution tests are performed in both space and time to determine the consistency and stability of solutions, and we ensure that energy is conserved to within 1% through each time step (Appendix B).

5. Results

We find four dynamic regimes of magma chamber evolution. Chambers of any size tested are unstable in many cases, either “freezing” or “erupting” (pressure exceeds the critical overpressure), due to an insufficient or excess melt flux rising from the base of the crust, respectively. However, there are parameters for which chambers rapidly reach a stable size (steady state) as long as melt supply is constant. There is also a “runaway growth” regime, in which viscous relaxation prevents chamber deviatoric stresses from growing while melt influx is still high enough for chamber growth. This regime is rendered finite in most cases, because wall-rock viscosities are bounded from below by the solid-liquid transition, which limits the stress relaxation timescale.

Typical snapshots of the simulations are shown in Fig. 4. Fig. 5 shows an example time evolution of volume. Model results for all parameter choices are compiled in dimensionless “stability field” representations for amphibolite and tonalite average crustal compositions in Figs. 6 and 7. To make compilations, each run is averaged temporally in these parameters (change in melt fraction, overpressure, shell viscosity, melt flux received by the chamber), and the dynamic results of the run are expressed in terms of averages. Each point on Figs. 6 and 7 corresponds to an averaged set of model runs, and is colored according to the end result.

Fig. 6 shows the stability field in terms of initial chamber size and melt flux through the crust. Fig. 7 plots the same data, but cast in terms of physical timescales. The abscissa is the total number of time steps in a given run. Small values indicate that the final result occurred very quickly, and represents a thermally or mechanically unstable system. Values approaching 10^6 years represent a thermally stable system. The ordinate is a ratio of average elastic and average viscoelastic timescales (Table 1). Large values (generally >1) represent systems that are viscously dominated, with a low shell viscosity. Systems with small values of this ratio (generally <1) are elastically dominated, growing

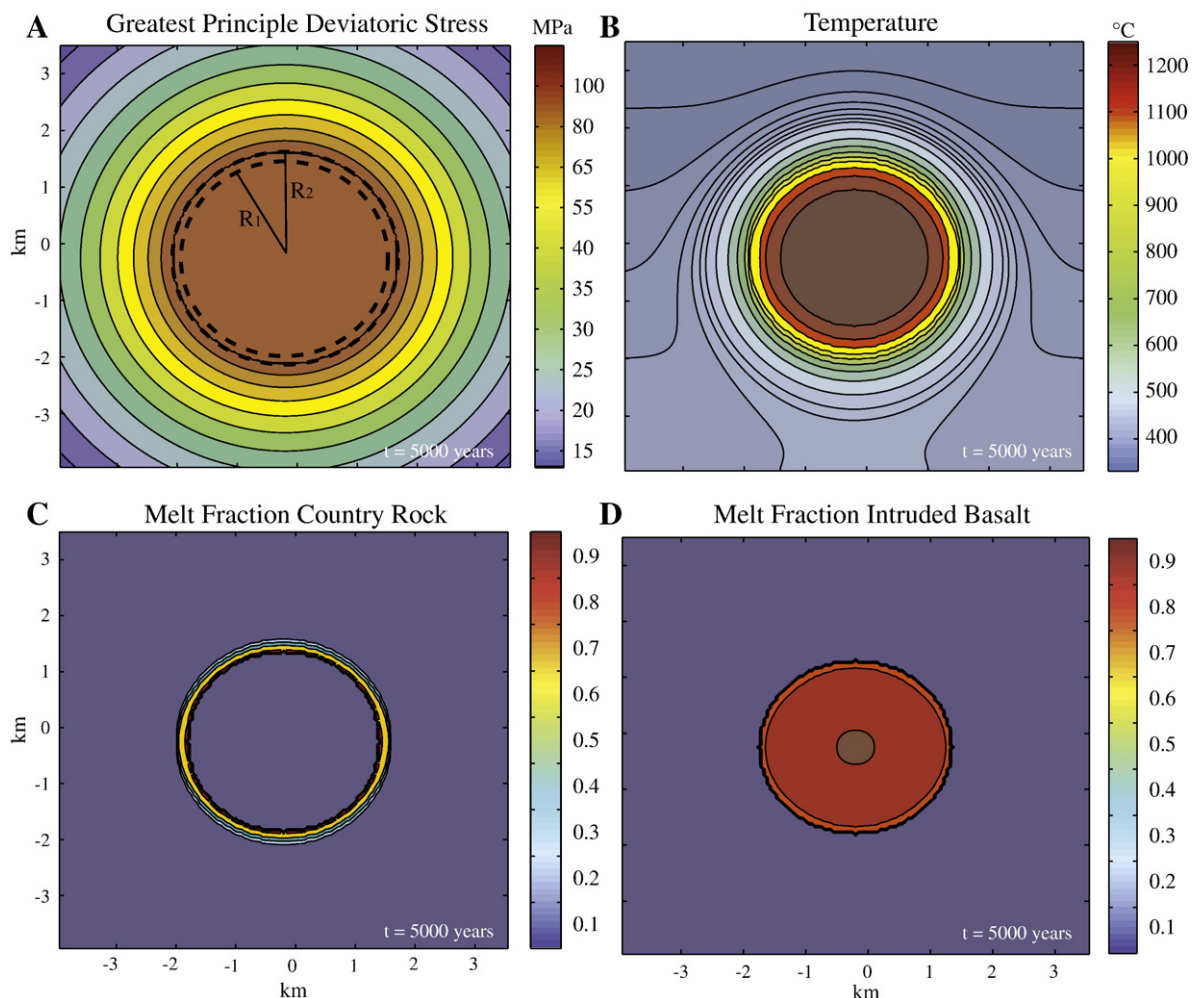


Fig. 4. 5000 years into the evolution of a 1 km initial radius chamber at 40 km depth. The intruding basalt is hydrous, the country rock is amphibolite, and the chamber is in a “stable” dynamic regime. Distance scale is the same in all panels and represent half the total numerical domain of the calculation. A) Maximum principle deviatoric stresses around the chamber. Focused dikes propagate orthogonal to plotted contours. The threshold stress of 1 MPa occurs outside the panel window. B) Temperature field. An initially static geotherm is perturbed by the presence of a hot chamber, resulting in reverse temperature gradients near the bottom of the chamber. C) Fraction of country rock melt around magma chamber, showing circular binning of melt around chamber. D) Fraction of intruded basaltic melt.

and pressurizing in response to melt influx. Because of the nonlinear melt fraction curves used (Appendix B), there are compositional differences between the lines dividing elastically- or viscously- dominated dynamics, such that $\tau_e/\tau_{ve} = 1$ does not strictly define regimes in Fig. 7. This representation does separate the model results, however, and is useful for deciphering which set of processes determines the outcome in a given run.

5.1. Dynamic regimes of chamber evolution

5.1.1. Frozen chambers

In the case of chambers that freeze, melt volume supplied by dikes in each time step (500 years) is a small fraction of the chamber volume, and does not supply enough enthalpy to prevent progressive solidification. Such a situation is aided by a net negative volume change of solidifying magma, which causes under-pressurization of the chamber and negative work, although it incurs a positive latent heat contribution to the enthalpy balance (Eq. (8)). Mechanically, the decrease in pressure decreases the capture radius of the magma chamber (Fig. 1), and hence the chamber focuses less melt from dikes. Progressive cooling of wall rocks (and hence progressive increase in wall rock viscosity) in a slowly solidifying chamber also feeds this process; because of the assumption

of an Arrhenius-type viscosity, this effect is exponential in time. Freezing thereby constitutes a negative feedback loop. In our model, chambers that receive less than $\sim 10^{-4} \text{ m}^3/\text{m}^2/\text{yr}$ melt flux freeze irrespective of size or depth in the geotherm, although smaller and shallower chambers are slightly more susceptible to freezing. As is exemplified in Fig. 5, deeper chambers generally freeze-out more slowly than shallow chambers, although the stochastic nature of melt supply causes some exceptions to this rule.

5.1.2. Erupted chambers

Chamber eruption is caused by exactly the opposite feedback processes. In this case, enthalpy supplied by dikes balances heat lost by conduction, and high melt influx results in rapid chamber expansion. If expansion and pressurization is larger than the rate of thermal diffusion, no viscoelastic shell forms and the chamber erupts on the elastic pressurization timescale. Likewise, eruption occurs if a shell exists but chamber pressurization occurs more quickly than the viscoelastic timescale. Net melting results in positive volume change, and hence positive work, with positive chamber overpressurization and negative latent heat. Magmatic lensing is amplified, resulting in a larger influx of magma. Such feedbacks lead to very high overpressures, and chamber rupture can occur on short timescales (Fig. 7).

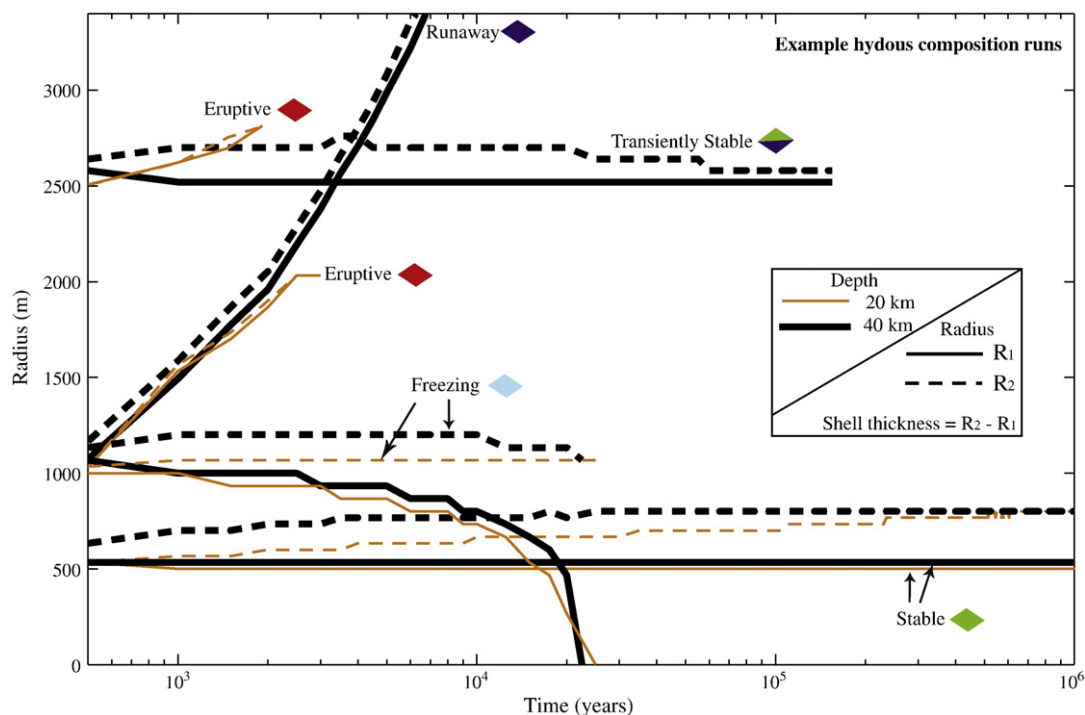


Fig. 5. Time evolution of inner and outer chamber radii (R_1 and R_2 in Fig. 1) for selected pairs of “wet” composition runs at 20 and 40 km depths (circled in Fig. 6). Growth of a viscoelastic shell ($R_2 - R_1 > 0$) is necessary for chamber stability, and chambers in the “eruptive” regime often expand more quickly than this can occur. 40 km deep chambers (thick as opposed to thin lines) grow viscoelastic shells more quickly than their 20 km depth counterparts. Labels indicate dynamic regime.

Chamber eruption occurs in most model runs if the flux is sufficiently high (greater than $\sim 10^{-1} \text{ m}^3/\text{m}^2/\text{yr}$), and are represented by red symbols in Figs. 6 and 7. However, eruption is a strong function of depth and size: larger, deeper chambers are the most stable (Fig. 6).

Red–blue symbols in Figs. 6 and 7 denote a transitionally eruptive regime in which chambers progressively freeze, but sometimes erupt before the inner radius shrinks to zero. This occurs because freezing is accompanied by an (exponential) increase in shell viscosity. Chambers that receive sufficient melt influx to pressurize significantly despite progressive solidification may then erupt as the shell viscosity increases. These results are run-dependent.

5.1.3. Stable chambers

Dynamic equilibrium is achieved for model runs that balance the competing dynamics, with $Pe \sim 1$ and $\tau_e/\tau_{ve} \sim 1$ (Eq. (5) and Table 1). There are both a temporally stable and a transient or unstable regime in which this occurs. Stable equilibrium results when chamber growth decreases asymptotically until subsequent volume changes are less than 0.5% of the chamber volume, and deviatoric stresses relax in the viscoelastic shell. These results are represented by green symbols in Figs. 6 and 7. Such chambers necessarily have an average elastic timescale larger than the Maxwell time (Fig. 7), and grow thick viscoelastic shells (Fig. 5) – although this thickness is composition dependent. Amphibolite melts past the critical melt fraction more readily than tonalite, so shell thicknesses are smaller in these settings. Total melt volume of both country rock plus basaltic magma (i.e., the chamber volume) remains approximately constant in time (Fig. 8), but melt fraction of country rock increases. In fact, large assimilation of country rock occurs primarily in stable chambers. Progressive heating of the domain does ultimately make this stable period finite, as does the slow build-up of stresses in some cases.

5.1.4. Runaway chambers

Transient dynamic equilibrium, or “runaway growth,” occurs when the elastic pressurization timescale is smaller than the thermal diffusion time (Table 1), such that chamber growth occurs in each

time step but the ratio of pressurization time to Maxwell time is near unity (Fig. 7). This results in deviatoric stress relaxation, however, continued melt influx causes the slow but continuous build-up of these stresses. Enthalpy is supplied to the system through dikes in large enough quantity that growth exceeds solidification. Such dynamic equilibrium is a “runaway growth” regime, and can result in rapid growth of chambers. However, the build-up of deviatoric stresses over long times (up to $\sim 100 \text{ ka}$ for amphibolite, slightly longer for tonalite) due to the continued influx of largely incompressible fluid into the chamber results in eventual chamber rupture.

This runaway growth regime is a direct result of the nonlinearity built into our model system by the imposition of a critical melt fraction, which places a lower bound on the magnitude of the wall rock viscosity, and hence an upper bound to the relaxation of stresses in the viscoelastic shell. Model runs in which runaway growth was accompanied by increasing shell stresses are represented by purple-red colored symbols in Figs. 6 and 7; runs in which growth was not accompanied by significant build-up of shell stresses are colored purple or purple-green (depending on whether the results were run-dependent). Some stable cases may still eventually erupt, however, because finite numerical domain width precludes assessment of a possible final chamber size for some of these fastest growing transient equilibrium model runs. Maximum average growth rates are $\sim 0.004 \pm 0.0005 \text{ km}^2/\text{yr}$, implying that a chamber may grow from 1 km radius to 10 km in $\sim 100 \text{ ka}$. This is roughly of the same order as the timescale for deviatoric stresses to become large, thus 100-fold increases in magma chamber volume are realistic in this system, provided that lower crustal melt flux is constant over this period.

5.2. The effects of magma and country rock composition

We find that, all else equal, magma chambers operating in each end member compositional scenario differ substantially in final behavior. The tonalitic proxy composition, defined by Eq. (60), contains less modal hydrous minerals, and has a correspondingly higher solidus and liquidus (Appendix B). Seismic velocities of the lower crust are more consistent

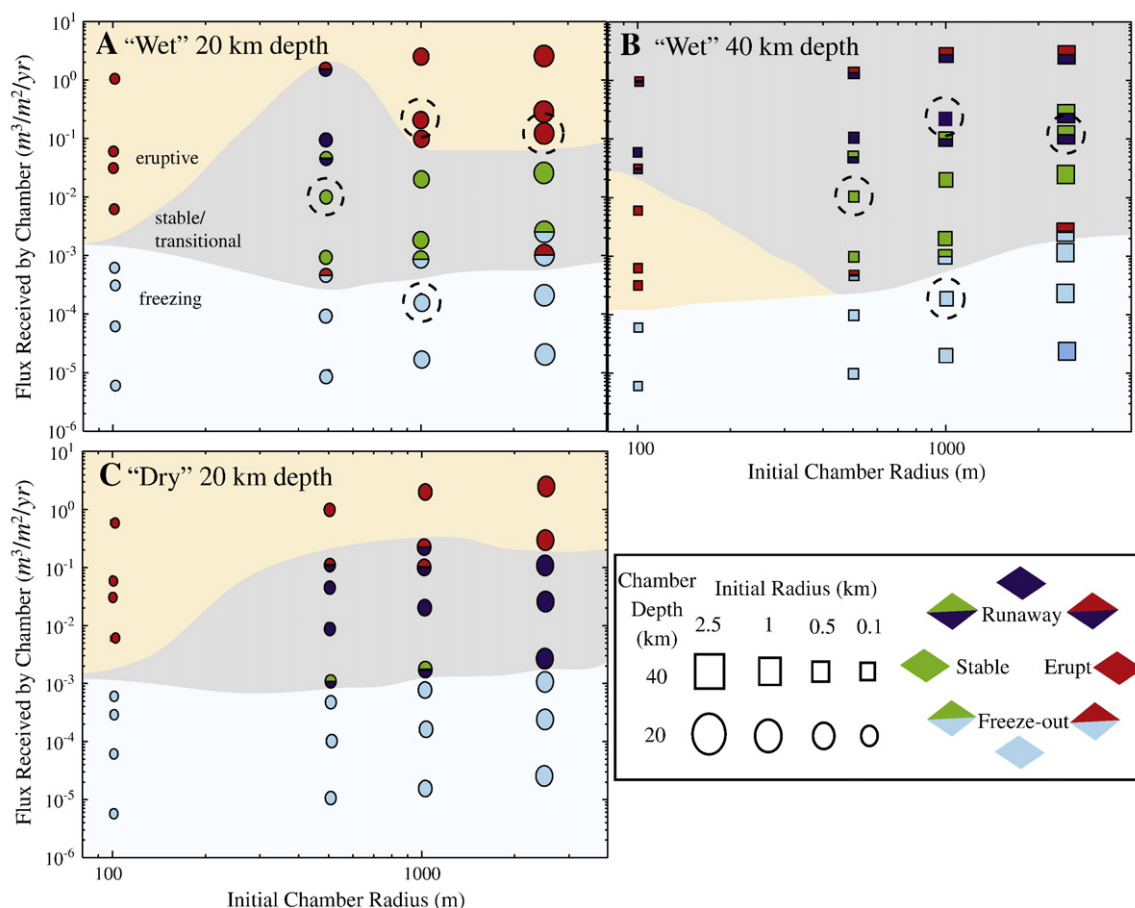


Fig. 6. Stability field representation of the parameter space, with initial chamber volume plotted against lower crustal melt flux. A) 20 km depth “wet” chambers. B) 40 km depth “wet” chambers. C) 20 km “dry” chambers. Solid colors represent results in which one dynamical regime dominates, while two-toned points represent runs in which the outcome was influenced by two interacting processes or was run-dependent (due to the stochastic simulations). These two-toned points sample the transitional states of the system, where competing physical processes are balanced. Circled points are plotted in Fig. 5, while shaded regions sketch qualitative boundaries between eruptive, stable/transitional and freezing regimes.

with an amphibolite-like composition grading to granulite facies in arc settings, while tonalite grading to granulite is expected in continental environments (Christensen and Mooney, 1995). In our simulations, chambers in tonalitic country rock are less stable than their “wet” counterparts, having little to no equilibrium regime, both freezing and erupting more quickly. In addition, these chambers melt more crustal material, leading to thicker viscoelastic shells. Crustal melting in the “runaway growth” regime is responsible for inhibiting “equilibrium” chambers (Fig. 6), and it is this large degree of crustal anatexis that is the most significant difference between the compositions.

Assimilated percentages are measured with respect to the magma that reaches the chamber and do not necessarily represent the total fraction of assimilation in crustal melt, as dikes that are not captured by a magma chamber leave the system in our model. The total crustal melt does not exceed ~40% by volume of intruded magma, consistent with other studies that invoke other mechanical processes (e.g. crustal extension (Hanson and Glazner, 1995)) to localize and maintain the mafic enthalpy to assimilate large volumes of crust. Stable chambers in a bulk amphibolitic country rock can assimilate up to ~50% by volume of their surroundings as melt, whereas the same chamber in a tonalitic environment may assimilate more, up to ~60–70%.

This difference may be attributed to the sharp step in the melt fraction curve (Eq. (60)) associated with the melting of plagioclase feldspar (Appendix B). Prolonged heating of tonalite will therefore produce a higher melt fraction shell than similar heating of amphibolite, over the range of 850–950 °C. A significant volume of tonalite country rock melts completely in the “runaway growth” regime chamber, and thus can initiate a switch from a predominantly mafic magma chamber

to a mostly felsic – but still high melt fraction – chamber as the anhydrous basalt with its higher solidus and liquidus slowly cools. Chambers that assimilate large fractions of crust need a large supply of enthalpy. Because there are dynamically stable chambers within a range of lower crustal melt flux (Fig. 6), the average percentage by volume of total crustal melt in a stable chamber is ~20% for our “wet” compositions, and ~40% for “dry” compositions.

Examples of the difference between anatexis “wet” and “dry” settings are illustrated in Fig. 8. While by no means an exhaustive parameter space search, these curves are nonetheless representative of the controls exerted on chamber melting by a combination of depth, melt flux, composition and initial size. It is evident that composition plays a leading role in assimilation of country rock, although melt flux is still the most important parameter, as it sets the space of stable and runaway chambers in which significant melting can occur.

The water content of the intruded magma also plays an important role in long-term chamber evolution. While we choose a relatively narrow range of basaltic compositions with 0 and 2 wt.% H₂O as dike material, compared to the upper observed limits of up to ~6–8 wt.% water in arc settings (Wallace, 2005), the melt fraction curves of these choices are notwithstanding quite different (Appendix B). We emphasize that the one-parameter melting curves in our model are proxies for real rock melting behavior, which will have different modes and hence a more complicated melting process.

Because we consider end member compositional scenarios in which “wet” basalt is paired with “wet” country rock and “dry” basalt is paired with “dry” country rock, it is natural to expect that our results represent end member dynamical regimes. The fact that we do

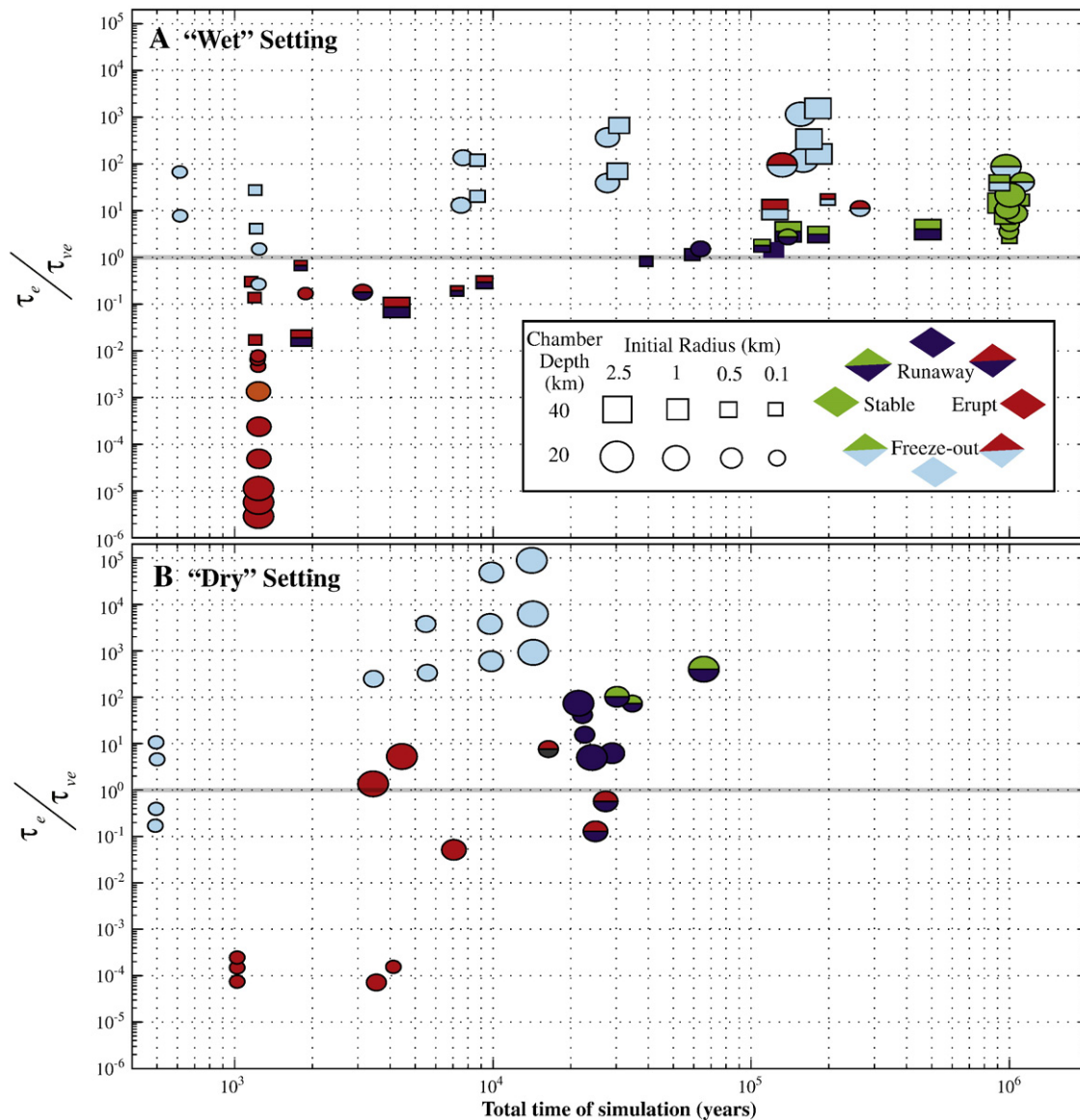


Fig. 7. Stability field representation of the parameter space, in terms of dimensionless physical timescales. The system's thermal stability (total run time) is plotted against a ratio of the chamber's average elastic (τ_e) and viscoelastic (τ_{ve}) timescales (Table 1). Chambers in different dynamical regimes (defined in the legend) separate in this representation, indicating that rheology and long-term stability are strongly coupled with a major dynamical transition occurring when $\tau_e/\tau_{ve} \sim 1$ (marked with a thick grey line), with deviations a result of the different nonlinear melt fraction curves (Appendix B). A) Hydrous "arc" setting runs (64 total). B) Anhydrous "continental" setting runs (32 total).

find significantly different long-term behavior of chambers in these scenarios, however, is an indication that composition does have a significant effect on magma chamber evolution, and that chambers in more anhydrous environments will tend to be less stable and less long-lived (at least at high melt fraction). It is possible that large magma bodies may exist for long time periods at low melt fraction (e.g., Bachmann and Bergantz, 2003; Huber et al., 2009). Because we end our simulations when the liquid-like portion (melt fraction > 0.6) of the magma chamber freezes, this is a scenario we cannot address. In both compositional cases, time evolution results in a bulk density that decreases in time, in accord with the differentiation and mixing processes that are taking place (Eqs. (64)–(66)). Short-lived chambers do not experience significant density evolution in our scheme.

5.3. Chamber pressurization and stress evolution

We use a numerical domain that is ~10 times the chamber diameter, so that melt flux reaching the chamber at the start of each run is much less than the total. However, continued pressurization and

growth of the magma chamber increase its capture radius, thereby focusing more melt from a larger region. Underpressurization or net freezing of the chamber decreases the capture radius and the amount of melt focused. Because of the assumed 15% volume change that accompanies melting or solidification (Dobran, 2001), large pressures are induced by melting and freezing of magma, and this acts in concert with rheological effects to amplify or damp elastic pressurization stresses (Fig. 10). Without consideration of these effects (including the threshold rupture criteria), chamber overpressures reach unrealistically high values that approach lithostatic, as illustrated for a chamber with an evolving shell of 100–300 m in Fig. 10. Chamber pressurization also affects the energy balance, and hence thermal evolution, through the work term in Eq. (8) that accounts for work due to melting or solidification at each time step. However, evaluation of this effect shows that it contributes little to the total energy budget, on the order of a few percent at each time step.

As is discussed in Jellinek and DePaolo (2003), the most important aspect of viscoelastic rheology around magma chambers is to relax stresses that might otherwise rupture the chamber and generate

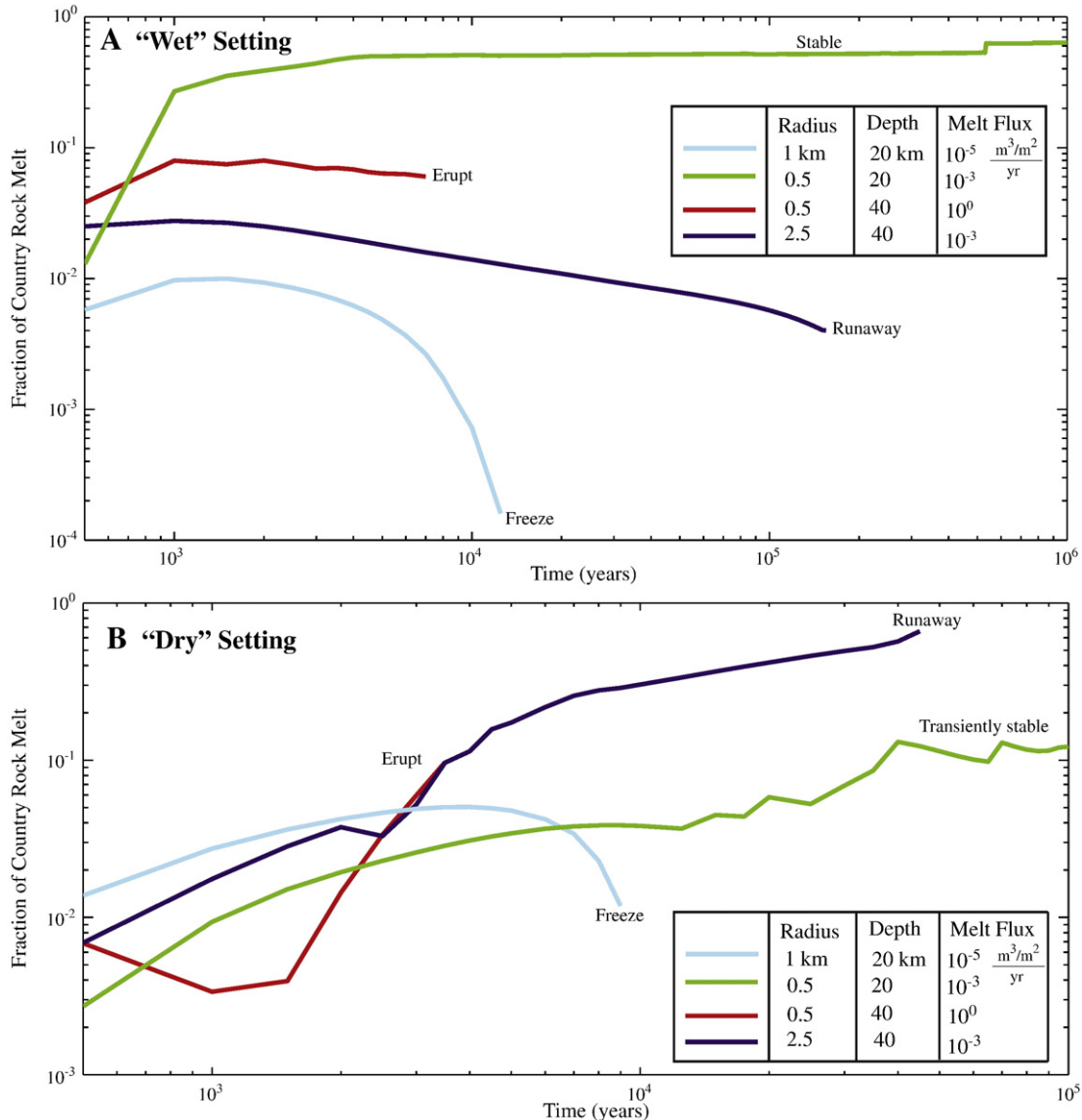


Fig. 8. A) Four examples from hydrous “arc” setting runs, to illustrate the degree of crustal anatexis and assimilation associated with each dynamical regime. Maximum country rock melt for this compositional suite occurs for chambers that are in the “stable equilibrium” regime, and is ~40–50% of the liquid chamber volume. B) The same examples, but from anhydrous “continental” setting runs. In this case, much more melting and assimilation can occur (see melt fraction curves Eqs. (58)–(62)), especially in the “runaway growth” regime. These chambers may assimilate up to ~60–70% by volume crustal melt.

volcanic eruptions. This is the process responsible for the “stable equilibrium” regime of chamber growth, but strong coupling to the thermal evolution of the shell means that the dynamics are time dependent. It is possible for viscoelastic effects to “shut off” as well as “turn on” chamber rupture. The blue–red symbols in Figs. 6 and 7 denote this behavior. However, temperature affects deviatoric stresses in a doubly exponential manner, through the relaxation timescale τ_{ve} (e.g., Dragoni and Magnanensi, 1989) and the temperature-dependent viscosity law (Eq. (63)):

$$\sigma_{dev}(\mathbf{x}, t) \sim \sigma_{dev}(\mathbf{x}) e^{-t/\tau_{ve}} \sim \sigma_{dev}(\mathbf{x}) e^{-t(EA^{-1} e^{nRT(\mathbf{x},t)/Q})} \quad (10)$$

where $\sigma_{dev}(\mathbf{x}, t)$ is the deviatoric stress at position vector \mathbf{x} and time t , E is the Young’s modulus of chamber wall rocks, $T(\mathbf{x}, t)$ is temperature, and all other constants are defined in Appendix B. The viscosity used to define the viscoelastic timescale τ_{ve} in Eq. (10) is strictly a function of both stress and temperature, however, the doubly exponential effect of temperature will dominate, such that deviatoric stresses relax in a narrow temperature range. This feature of the stress evolution may have

implications for the possible timescales of eruptibility, as dike propagation (in our formulation) will not occur to drain the chamber. To erupt such a chamber, other processes (such as volatile exsolution, roof collapse or external triggers) not considered here must operate.

5.4. The effects of depth

For magma chamber stability, the proximity of a stress free surface has two major effects. The first is to concentrate deviatoric stresses on the sides of the chamber (e.g., Pinel and Jaupart, 2003; Grosfils, 2007), which acts to destabilize the chamber and promote ring fracture formation. The second is to modulate the capture radius of the chamber, which upon shallowing exhibits a decrease, and then a sharp increase in the immediate vicinity of the free surface (Karlstrom et al., 2009). For chambers surrounded by viscoelastic country rocks, both of these effects are time dependent.

This is illustrated in Fig. 9, for choices of chamber size ($R_1 = 1$ km, $R_2 = 1$ km), depth (5 km), shell viscosity ($\nu = 10^{19}$ Pa s) and overpressure ($\Delta P = 100$ MPa) that emphasize the differences between this case

and the symmetric overpressure solutions in an infinite medium. The free surface generally begins to affect normal stress concentration at the wall of an elastic chamber when the ratio of depth d to radius R satisfies $d/R < 3$ (Grosfils, 2007). However the time evolution of viscoelastic stresses (plotted in Fig. 9A as the first stress invariant) makes the surface effects more pronounced because the effective normal stress boundary conditions expand in time (Appendix B). The capture radius begins to be significantly affected at depths more shallow than 20 km for the small chambers we consider here (Fig. 9B).

Because of the added complexity of near-surface effects, and the complexity of the analytical half-space solution (Eq. (41)–(46)), we leave a more complete parameter search of shallow chambers for future work. For the 20 and 40 km depth chambers, additional stress concentrations due to free surface effects are less than 15%, and would not change the results significantly. However, we have run a number of test cases at shallow depths to explore the general trends. Picking the same initial size and melt flux as in Fig. 5, we find that the effect of decreasing depth is generally to inhibit the stable regimes of chamber growth. For example, a “wet” composition run using 1 km initial radius, $10^{-3} \text{ m}^3/\text{m}^2/\text{yr}$ melt flux (which is stable 20 and 40 km depths in Fig. 6) enters an eruptive regime at 10 km depths. This is due to the stress concentration effects (easier to rupture a chamber) and the cool country rocks (higher shell viscosity, more solidification).

We anticipate that a more thorough study of these effects may have applications to the conditions for caldera-forming chambers, and to active shallow volcanic areas, where ground deformation measurements (e.g., Newman et al., 2001) provide insight in to short-term chamber dynamics. Within the framework of our model, geodetic measurements may be inverted not only for chamber geometry and pressure, but for lower-crustal melt flux and dynamic regime (which bounds the active lifetime).

6. Discussion

6.1. Summary of model results

It will be useful in the following discussion to summarize model results in terms of the four dynamical processes of interest laid out in the introduction.

1. Rheological and stress evolution associated with long-lived high melt fraction systems in a geothermal temperature gradient.

The development of a viscoelastic shell around magma chambers has a profound effect on their long-term dynamics. The ratio of elastic to viscoelastic timescales governs the relaxation of deviatoric stresses that prevents chamber rupture. By coupling this process to the thermal evolution of a magma chamber, and to particular parameterizations of rock composition, we find that such temperature-induced rheological changes are strong functions of the local geotherm and composition. Deeper chambers and chambers surrounded by more felsic country rocks generally have the greatest rheological impact on their surroundings.

2. Average compositional evolution of the magma chamber and assimilation of country rock.

In our simplified treatment of magma chamber processes, we are unable to address the details of compositional evolution within the chamber (e.g. Gerya et al., 2004). However, we do address crustal assimilation, and find that melting of country rocks by magma chambers is a strong function of their composition and water contents. We find assimilated tonalitic country rock of up to ~70% the total chamber volume in “runaway growth” chambers (Fig. 8). Amphibolitic end member chambers, on the other hand, assimilate up to 50% by volume country rock only in the “stable” regime. We note that these are the extreme values of crustal melting that are achieved over long periods of

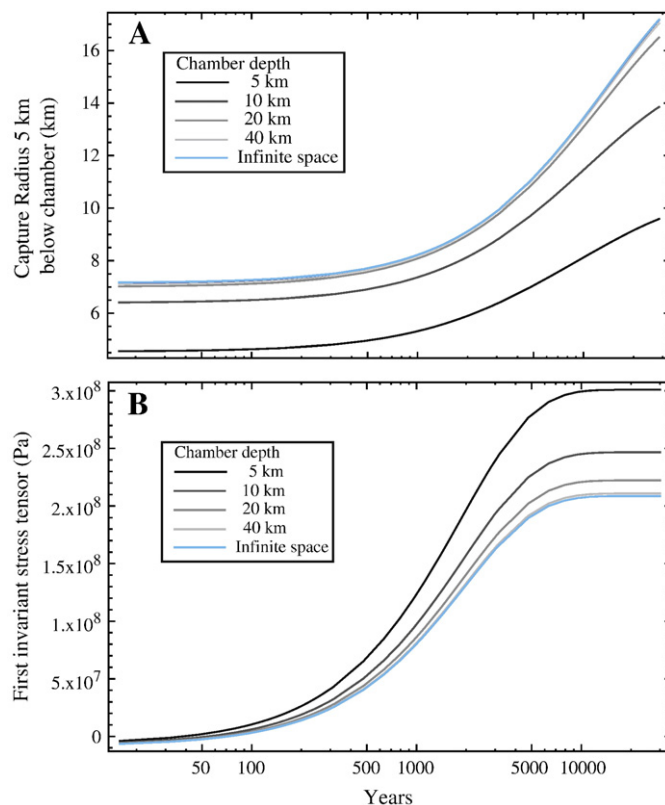


Fig. 9. A) Time evolution of capture radius (Fig. 1) for chambers at different depths. Note that the capture radius increases in time due to viscous creep in the shell, and that the half space solutions approach the infinite space solution as depth increases. B) Time evolution of the maximum first invariant of the stress tensor evaluated at R_1 , comparing normal stresses between the half space and infinite space solutions in a coordinate-independent way. Normal stresses around shallow chambers are markedly higher in magnitude than deep chambers, and we note that the position of maximum stress on the boundary R_1 shifts with depth as well.

continued enthalpy supply without eruption. “Freezing” or “eruptive” chambers rarely assimilate more than a few percent by volume of country rock (Fig. 8), which may be considered to be more average.

3. Stability of the system: will the magma chamber rupture, freeze, or exist in dynamic equilibrium within the crust for the lifetime of constant melt supply?

The stability of magma chambers is governed primarily by lower crustal melt supply (Eq. (6)). Melt flux smaller than $\sim 10^{-4} \text{ m}^3/\text{m}^2/\text{yr}$ does not transport enough enthalpy to thermally sustain magma chambers, and these chambers freeze in all cases. The range of stable chambers is a function of depth and composition, but encompasses melt fluxes consistent with the upper estimates of melt flux in arc settings ($\sim 10^{-3} \text{ m}^3/\text{m}^2/\text{yr}$), which is also comparable to the average melt flux per kilometer of mid-ocean ridge, e.g., Chen (1996). We emphasize that a more three dimensional treatment of this problem will almost certainly decrease this stable range of melt flux, because chambers will both lose more heat via conduction and focus rising melt more efficiently in three dimensions. Chamber eruption is found for melt flux exceeding $10^{-1} \text{ m}^3/\text{m}^2/\text{yr}$ in most cases, however, deep chambers with an initially large size are less sensitive to large melt influx, and may be in the “runaway growth” regime for melt fluxes of this magnitude. Mantle plume-scale melt flux may therefore, in principle, sustain rapid but stable growth of deep-seated magma chambers, and magmatic lensing provides one mechanism by which large radiating dike swarms associated with these features (Ernst et al., 1995) might be emplaced.

4. The possibility for large-scale growth of a high melt fraction reservoir.

The “runaway growth” regime of magma chambers depends critically on both a sufficiently high melt flux, and a shell viscosity that remains low enough to relax the large stresses generated by this melt influx. Runaway growth, therefore, depends greatly on depth and composition. Magma chambers in tonalitic country rocks are more prone to this behavior, but large scale growth occurs for some range of parameters in all of the depths and compositions tested in this study. This growth may occur very rapidly, with 100-fold volumetric increases in 100 ka, but will likely be shut off by shell viscosities that can no longer relax chamber stresses.

6.2. Application to terrestrial magmatic systems

The construction of large igneous intrusions in the Earth's crust has been argued to result from either diapir-dominated or dike-dominated transport processes (Petford, 1996; Miller and Paterson, 1999). We assume here that the latter is more realistic, although the two may share significant similarities, and base our arguments on 1) the short dike rise timescale compared to the Stokes velocity of a melt diapir in the crust, and 2) the mechanism of magmatic lensing, whereby a stalled pressurizing inclusion of melt may focus rising melt to attain a large volume. There is considerable field evidence to support dike transport of melt in middle to lower crustal terrains (e.g., Jagoutz et al., 2006; Dumond et al., 2007), but kilometer scale viscous advective processes have also been inferred (e.g., Zak and Paterson, 2005). While we cannot hope to address specific field observations and analytical studies directly with the simplified modeling framework presented here, general features of magmatic transport processes and timescales may be constrained.

Predictions of our model include chamber growth rates, bulk assimilation of crustal rocks, and constraints on lower crustal melt flux needed to produce stable and/or large chambers. The broad dynamical regimes of chamber evolution that result are physically general, and should translate to real intrusions. In this framework, it is interesting to ask whether various classes of intrusion (e.g., calderas, plutons, layered mafic intrusions) might be differentiated by dynamic regime alone. In addition, we would like to point out some specific measurements of transport processes that our modeling addresses.

6.2.1. Caldera-forming chambers

Calderas are the best geologic evidence for large (up to ~100 km scale) high melt fraction crustal magma chambers, and are the center of much controversy regarding spatiotemporal pluton-volcano connections (e.g., Lipman, 2007; Glazner et al., 2008). While there are many complementary ways to approach this problem, remote sensing of deformation in calderas provides important constraints on processes that are difficult to obtain from the rock record. For example, Newman et al. (2001) model surface deformation at Long Valley caldera assuming inflation is due to an inflating shallow magma chamber with a viscoelastic shell. They infer a shell viscosity ($\sim 10^{16}$ Pa s) that is much lower (and perhaps more realistic) than our estimated bound on wall-rock viscosity ($\sim 10^{19}$ Pa s, Appendix B), especially for shallow chambers in a normal geotherm. Our modeling indicates that the size of viscoelastic shell is composition- and depth-dependent, with $1 \leq R_2/R_1 \leq 2$ for tonalitic country rocks, and $1 \leq R_2/R_1 \leq 1.5$ for amphibolite in deeper chambers, and generally very small for 5–10 km deep chambers. In fact, because shallow stable or runaway chambers are very difficult to achieve in a “normal” geotherm, we suspect that the crust must be pre-warmed to form large, high melt fraction bodies in the shallow crust.

Because constant magma addition increases chamber overpressure to values that approach lithostatic in a purely elastic model, rupture will occur unless chamber stresses are relaxed. Indeed, as demonstrated in Fig. 10, the use of purely elastic pressurization as a proxy for magma chamber dynamics both results in unrealistically large overpressure and misses important time-dependent dynamics (Results section). We note that the “runaway growth” regime of magmatic lensing accommodates chamber growth in 10^5 – 10^6 year, which is similar to the range of

timescales postulated in other studies of caldera-forming eruptions (e.g., Hanson and Glazner, 1995; Bachmann and Bergantz, 2003; Simon et al., 2008). Caldera roof collapse depends on the concentration of deviatoric stresses and the development of ring fractures (e.g., Gudmundsson, 1988). If the wall rocks are viscoelastic (Eqs. (41)–(46), Fig. 12) the concentration of these stresses occurs only after ~ 1 Maxwell time, suggesting a lag between melt pressurization and collapse in caldera-forming eruptions (Fig. 9b).

Hughes and Mahood (2008) compile a database of calderas around the Pacific Rim, finding that calderas are typically found in regions of local compressive tectonic stresses. This may be explained through consideration of the mechanical aspects of magmatic lensing (Karlstrom et al., 2009), whereby the capture radius of the chamber (and therefore the incoming melt flux) is increased with background compressive stresses. As pointed out by Jelinek and DePaolo (2003), extensional stresses promote storage of an already-existing magma chamber by providing strain to accommodate melt influx and decrease chamber overpressures. However, for small chambers, extension also serves to shut off the magmatic lensing mechanism by creating more horizontally oriented least compressive stresses and decreasing the capture radius of the chamber. This will inhibit the interaction of rising dikes with already-existing magma chambers. Hence it is possible that local tectonic extension may both inhibit the growth of small magma chambers and promote the stability of larger ones.

6.2.2. Plutons and layered mafic intrusions

Recent detailed geochronology indicates that some (and perhaps most) intrusive suites have crystallization histories of several million years e.g., the Tuolumne Intrusive Suite and Mt. Stuart Batholith, (Miller et al., 2007), and individual plutons may have been constructed over 1 Ma (Coleman et al., 2004). In the Sierra Nevada Batholith, plutons were emplaced at depths ranging from 5 km in the East (e.g. the Bridgeport “Low P” zone) to >25 km in the South and Southwest (Ague and Brimhall, 1988; Pickett and Saleeby, 1993). If we use directly modern estimates for arc melt flux as a proxy for melt flux at the time of emplacement of the Sierra Nevada Batholith, and assume intrusion depths of 20 km we find that it is indeed possible to achieve chambers in the stable equilibrium or freezing regimes

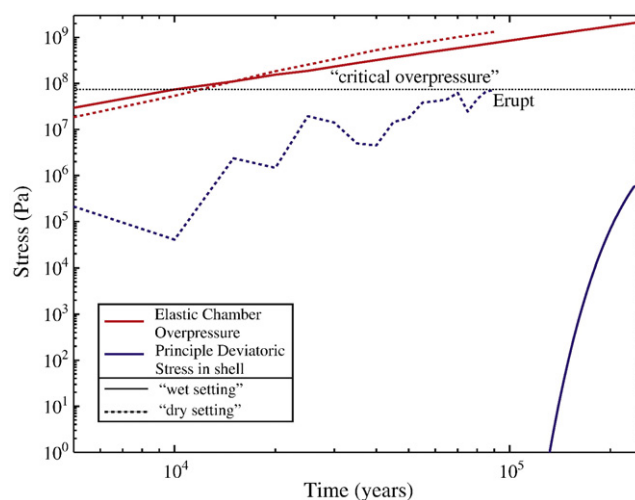


Fig. 10. Example time evolution of principle deviatoric stresses in the viscoelastic shell and “elastic” stresses for two chambers. Elastic stresses are presented for reference only, and are not used in our model. Composition is the only difference between the two cases, which begin with radii of 2.5 km and depths of 20 km. Variations in deviatoric stress for the “dry” setting run (dashed blue line) in part reflect the stochastic input of melt and enthalpy from dikes. These contributions may be negative (positive) for net chamber solidification (melting). The “wet” setting run gradually builds up deviatoric stresses over the course of the run, and thus represents a “runaway growth” regime.

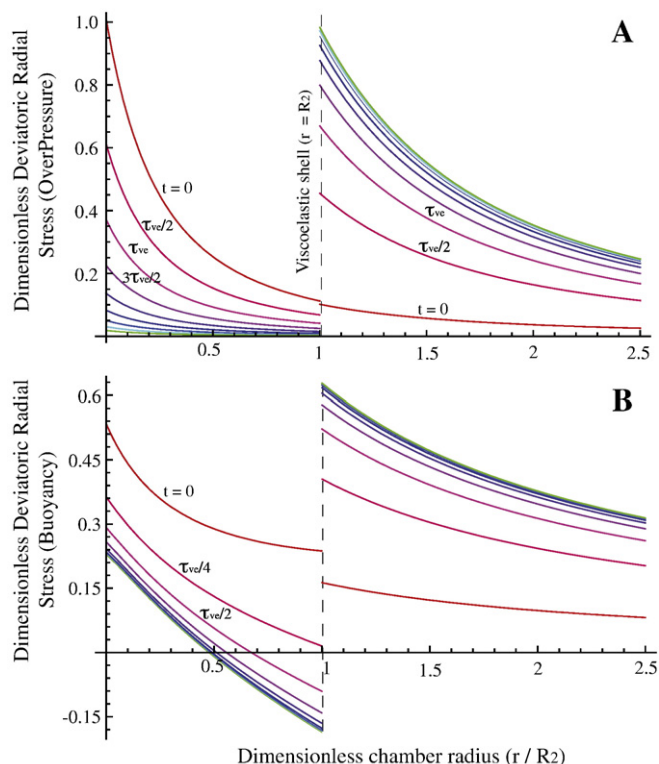


Fig. 11. A) Time evolution of greatest principle deviatoric stresses around a circular overpressured chamber in an infinite space (Eqs. (12)–(17)). Colored curves indicate time in increments of one half the Maxwell time ($\tau_{ve}/2$, Table 1), for a shell viscosity of 10^{19} Pa s. B) Time evolution of deviatoric stresses around a buoyant circular chamber. In this case, asymmetry in the boundary conditions induces incomplete relaxation of deviatoric stresses in the shell. Colored curves are time in increments of $\tau_{ve}/4$. Stresses in this case are evaluated at the top of the chamber $\phi = 0$ (the angle of maximum stress maximum for infinite space solutions of positive buoyancy). Normal stress boundary conditions are normalized to one in both panels.

(Fig. 6). Based on this evidence, it does appear possible that 1–10 km scale chambers could in principle exist at high melt fraction for extended periods (≥ 1 Ma). If the crust were prewarmed by previous episodes of intrusion, stable chambers, perhaps caldera-forming (de Silva and Gosnold, 2007), would be more likely in the shallow crust.

Particular examples of well-exposed pluton–country rock contacts in the Sierra Nevada offer other field evidence for the dynamic regimes of chamber growth. For example, the Jackass Pass pluton (McNulty et al., 1996) displays structural evidence for dike-assembled magma chambers and for ductile creep that would imply a rheological gradient at the chamber margin. Distinct absence of ductile flow markers and a sharp pluton–wall rock contact in the Piute Meadow pendant (Albertz, 2005) could be the result of a rapidly freezing intrusion, or chambers in a “runaway growth” or “eruptive” regime that expand without forming a viscoelastic shell. On the other hand, observations of increasing strain intensities toward the pluton in the Saddlebag Lake pendant (Albertz, 2005) are consistent with the development of rheological gradients. It seems clear that pluton assemblage is a complex and variable process, and that relic batholithic structures represent time-integrated portraits of multiple chambers in different dynamical regimes, associated with different and discrete volcanic centers, as high precision dating of plutons (Matzel and Bowring, 2006) and possible analog volcanic systems (de Silva and Gosnold, 2007) are beginning to suggest.

Layered Mafic Intrusions found in predominantly cratonic settings form another class of intrusions with which to compare our model. Based on estimates of total volume and emplacement time, Cawthorn and Walraven (1998) estimate that the Bushveld Complex (total volume $\sim 10^6$ km³) filled at an average rate of 9–15 km³/yr, and suggest that

eruptive removal of magma is required in order to fit the estimated cooling rates. By extrapolation to 2D using a spatial dimension of 100 km for the Bushveld, this volumetric influx rate is comparable to the highest melt fluxes that we model (10^0 m³/m²/yr), which are an estimate of mantle plume melt rates (Farnetani and Richards, 1995). This is a possible source for Bushveld melt (Hatton, 1995). Geobarometry on pelitic gneiss suggests that the depth of crystallization for at least part of the Bushveld Complex was ~ 20 km (Stevens et al., 1997; Johnson et al., 2003), though others have argued, based on geochemical evidence, for a deeper-seated “staging chamber” (e.g. Harris et al., 2005). Extensive isotopic analyses (e.g., Harris et al., 2005; Majer et al., 2000; Kruger, 2005) also suggest significant crustal assimilation, which may have reached upwards of 40% of the total melt volume (Harris et al., 2005).

Based on these observations, we speculate that the Bushveld magma chamber may have been in the “runaway growth” regime of our model. Leucosomes and migmatitic textures (Johnson et al., 2003) extend orthogonally into the country rocks 400–700 m from the intrusion, suggesting a lower bound to the viscoelastic shell around the chamber. If these estimates of shell thickness are correct and representative (even within an order of magnitude), this implies a very thin thermally altered region (less than 1% of the Bushveld’s North–South extent), and hence very rapid emplacement. Detailed thermal modeling of phase equilibria for the aureole beneath the Bushveld Complex (Johnson et al., 2003) result in a melt fraction–temperature parameterization that most qualitatively matches our tonalite curve for the range of melt fractions modeled in that study (≤ 0.3 volume fraction melt). Crustal assimilation similar to the 40% inferred for the Bushveld is quite possible in our model (Fig. 8), though we again stress that this is a qualitative comparison, as in particular our chamber geometry is highly idealized. If the Bushveld Complex represents a “runaway growth” regime magma chamber, the rapid emplacement of such a high volume chamber in the mid crust is quite possible in ~ 75 ka (Cawthorn and Walraven, 1998), and chamber rupture is an inferred consequence of this mode of emplacement.

6.3. Conclusion

Within the conceptual model developed here, we have shown that (1) there are four distinct dynamical regimes for chamber growth: long-lived (≥ 1 Ma) and thermally viable magma chambers are possible at a range of depths, as are thermally viable chambers that can rapidly grow, (2) viscoelastic properties of the coupled chamber/country rock system can “shut off” as well as “turn on” chamber rupture, and (3) magma chambers may assimilate a range of crustal rocks, depending on the dynamical regime. While most chambers in eruptive or freezing regimes will not assimilate more than a few percent by volume of crust, a narrow range of dynamically stable chambers may assimilate $>60\%$ by volume of the surrounding crust if the crust is relatively evolved and dry, and up to $\sim 40\%$ by volume for “wet” magma within amphibolitic country rock. These percentages are relative to the amount of melt reaching the chamber, and should not be necessarily considered to represent the bulk assimilated fraction of crustal melt, nor necessarily a firm characteristic of all long-lived chambers.

Comparison of our models to realistic systems is largely speculative at this stage, however we believe that highly disparate intrusive structures may be reasonably cast into a framework of dike-fed magma chamber growth. Our approach suggests that differences in magmatic intrusions worldwide are due to differences in local physical parameters and not physical processes. Lower crustal melt flux is the most important of these parameters, and this likely determines the overall stability and size of a given intrusion. However, crustal composition, background stresses and depth of emplacement are also important and may strongly modulate chamber behavior. In particular, the influence of tectonics will strongly affect the rise of magma through the crust, and indeed forms much of the framework for our understanding of volcanism generally (e.g., Canon-Tapia and Walker, 2004). Likewise,

interactions between magma chambers, dikes and multiphase fluid processes are ultimately responsible for surface volcanism, and a better characterization of topological evolution of the system will further our ability to link the rock record and other time-integrated evidence to magma transport physics.

Acknowledgements

We thank Mark Richards and Justin Simon for reading and commenting on an early version of this manuscript, and are indebted to John Wolff and Eric Grosfils for providing very thorough reviews. This research was funded by NSF EAR0608885 and NASA 08-MFRP08-0073 grants to MM.

Appendix A. Viscoelastic chamber stresses

We solve the equilibrium equations of Linear Elasticity (e.g., Fung, 1965),

$$\nabla^2 \mathbf{u} + \frac{1}{1-2\nu_{1,2}} \nabla(\nabla \cdot \mathbf{u}) = 0 \quad (11)$$

where \mathbf{u} are the vector elastic displacements, and $\nu_{1,2}$ is Poisson's ratio for the shell ($\nu_1 = 0.4$, to account for the presence of partial melt) and the country rocks ($\nu_2 = 0.25$). We assume that the Young's moduli inside and outside the shell are equal, $E = 70$ GPa. Subject to boundary conditions in Eqs. (1)–(4), we use the method of stress functions for which a general solution to the equilibrium equations in polar coordinates (r, ϕ) exists (Fung, 1965). Taking care to avoid multiple-valued displacements, stresses inside the viscoelastic shell are

$$\sigma_{rr,in}(r, \phi) = \bar{A}_1 - \frac{\bar{B}_1}{r^2} + \left(\frac{\bar{C}_1(2\nu_1 - 3)}{r} - \frac{\bar{D}_1}{r^3} + \bar{E}_1 r \right) \cos(\phi) \quad (12)$$

$$\sigma_{\phi\phi,in}(r, \phi) = \bar{A}_1 + \frac{\bar{B}_1}{r^2} + \left(\frac{\bar{C}_1(1 - 2\nu_1)}{r} + \frac{\bar{D}_1}{r^3} + 3\bar{E}_1 r \right) \cos(\phi) \quad (13)$$

$$\sigma_{r\phi,in}(r, \phi) = \left(\frac{\bar{C}_1(1 - 2\nu_1)}{r} - \frac{\bar{D}_1}{r^3} + \bar{E}_1 r \right) \sin(\phi) \quad (14)$$

and outside the shell, in the assumed elastic medium

$$\sigma_{rr,out}(r, \phi) = \frac{\bar{B}_2}{r^2} + \frac{\bar{C}_2(3 + 4\nu_1(\nu_2 - 1) - 4\nu_2) \cos(\phi)}{r} \quad (15)$$

$$\sigma_{\phi\phi,out}(r, \phi) = -\frac{\bar{B}_2}{r^2} + \frac{\bar{C}_2(1 + 4\nu_2(\nu_1 - 1)) \cos(\phi)}{r} \quad (16)$$

$$\sigma_{r\phi,out}(r, \phi) = \frac{\bar{C}_2(2\nu_2 - 1)(2\nu_1 - 1) \sin(\phi)}{r} \quad (17)$$

Here $\bar{A}_1, \bar{B}_1, \bar{C}_1, \bar{D}_1, \bar{E}_1, \bar{B}_2, \bar{C}_2$ are constants evaluated to satisfy the boundary conditions, Eqs. (1)–(4), and are found to be

$$\bar{A}_1 = (\Delta P(\nu_2 - \nu_1)R_1^2) / \mathcal{D} \quad (18)$$

$$\bar{B}_1 = (\Delta P R_1^2 R_2^2 (-2 + \nu_1 + 2\nu_2^2 - \nu_2)) / \mathcal{D} \quad (19)$$

$$\bar{C}_1 = (R_1^2 \Delta \rho g / 4(\nu_1 - 1)) \quad (20)$$

$$\begin{aligned} \bar{D}_1 = & -(R_1^4 R_2^2 \Delta \rho g (R_2^2 (1 + \nu_1 (1 - 6\nu_1 + 8\nu_1^2)) (3 + 4\nu_1 (\nu_2 - 1) \\ & - 4\nu_2) + 2(4\nu_1 - 3) (-R_1^2 (1 + 4\nu_1 (\nu_2 - 1) - 6\nu_2) (\nu_1 - \nu_2) \\ & + R_2^2 (2\nu_1 - 1) (-1 + \nu_2 + 2\nu_2^2)) \log(R_2)) / \mathcal{G} \end{aligned} \quad (21)$$

$$\begin{aligned} \bar{E}_1 = & -(R_1^2 \Delta \rho g (R_1^2 (1 - 2\nu_1) (1 + \nu_1) (3 + 4\nu_1 (\nu_2 - 1) - 4\nu_2) \\ & - 2(4\nu_1 - 3) (-R_2^2 (1 + 4\nu_1 (\nu_2 - 1) - 6\nu_2) (\nu_1 - \nu_2) \\ & + R_1^2 (2\nu_1 - 1) (-1 + \nu_2 + 2\nu_2^2)) \log(R_2)) / \mathcal{G} \end{aligned} \quad (22)$$

$$\bar{B}_2 = (\Delta P R_1^2 R_2^2 (\nu_1^2 - 2)) / \mathcal{D} \quad (23)$$

$$\begin{aligned} \bar{C}_2 = & -(R_1^2 \Delta \rho g (1 + \nu_1) (2R_1^2 R_2^2 (1 - 2\nu_1)^2 \\ & + R_1^4 (3 - 2\nu_1) + R_2^4 (3 + 2\nu_1 (-7 + 4\nu_1)) - 2(R_1^4 - R_2^4) \\ & \times (-3 + 4\nu_1) \log(R_2)) / \mathcal{G} \end{aligned} \quad (24)$$

where

$$\mathcal{D} = R_2^2 (2\nu_1^2 - \nu_2 - \nu_1 - 2) + R_1^2 (\nu_2 - \nu_1) \quad (25)$$

$$\begin{aligned} \mathcal{G} = & 4(\nu_1 - 1) ((R_1^4 + R_2^4 (1 - 4\nu_1)) (1 + \nu_1) (3 + 4\nu_1 (\nu_2 - 1) - 4\nu_2) \\ & + 2(R_1^4 - R_2^4) (4\nu_1 - 3) (2\nu_2^2 + \nu_2 - 1) \log(R_2)). \end{aligned} \quad (26)$$

These stresses are the two dimensional equivalent of the spherically symmetric viscoelastic solutions of Dragoni and Magnanensi (1989), but include buoyancy effects. Given these purely elastic solutions, it is possible to find viscoelastic solutions via the correspondence principle (Fung, 1965), in which we assume that the material in the region $R_1 < r < R_2$ behaves as a Maxwell solid only with respect to deviatoric stresses (e.g. Dragoni and Magnanensi, 1989):

$$\frac{1}{\eta_{wr}} \sigma_{dev} + \frac{1}{E} \frac{d\sigma_{dev}}{dt} = \frac{d\epsilon_{dev}}{dt} \quad (27)$$

$$tr \sigma = 3Ktr \epsilon \quad (28)$$

where K is the bulk modulus, ϵ is the strain tensor, and η_{wr} is the shell viscosity. The correspondence principle then entails making the substitution

$$\mu_1 = \frac{E}{2(1 + \nu_1)} = \mu_1(s) = \frac{\mu_1 \eta_{wr} s}{\mu_1 + \eta_{wr} s} \quad (29)$$

where s is the Laplace domain variable, and where use of the rigidity μ_1 as the sole time-varying material property indicates that only deviatoric components of the stress are subject to creep (Dragoni and Magnanensi, 1989).

Viscoelastic solutions are then found by taking the inverse Laplace transform of the stress components:

$$\sigma_{ij,VE} = \mathcal{L}^{-1}[\sigma_{ij,E}(s)]. \quad (30)$$

Here $\sigma_{ij,VE}$ are viscoelastic stresses, $\sigma_{ij,E}(s)$ are the Laplace-domain transformed elastic stresses, and \mathcal{L} is the Laplace transform operator

$$\mathcal{L}[f(t)] = \int_0^\infty e^{-st} f(t) ds. \quad (31)$$

The expressions obtained by performing the Laplace transforms are unwieldy and are not presented here. Cumbersome algebraic manipulations and inverse Laplace Transforms are performed with the symbolic mathematics software package Mathematica (Wolfram 2008).

Principle deviatoric viscoelastic stresses used in the model are then found by solving for the eigenvalues of the matrix defined by

$$\sigma_{dev,VE} = \sigma_{VE} - tr \sigma_{VE} \quad (32)$$

and are even more complicated expressions.

Of the two boundary conditions considered in this study, overpressure ΔP and magma buoyancy $\Delta\rho g$, overpressure is the most important, generating stresses that are 3–5 orders of magnitude greater than buoyancy effects. However, magma buoyancy is a first-order mechanism for magma transport in many situations. It is therefore of note that viscoelastic solutions for a uniformly pressurized circular cavity differ in important respects from corresponding buoyant solutions. The viscous response to an overpressured inclusion is isotropic, and a constant overpressure boundary condition in a viscous medium requires a constant divergence of mass from the center of the inclusion. Buoyancy effects are, however, not isotropic and generate flow around the inclusion.

Our model considers a circular chamber with a viscoelastic shell in an elastic medium, which acts as a rigid container on the Maxwell timescale of the shell. Deviatoric stresses due to chamber overpressure relax in time because of the isotropic nature of the viscous response – in fact, this property defines pressure. However, deviatoric stresses due to buoyancy do not. This is illustrated in Fig. 11, where the time-dependent deviatoric radial stress at the top of the chamber ($\phi=0$) is plotted for the overpressure and buoyancy boundary conditions. While stresses due to overpressure decay to zero in time within the shell, buoyancy stresses approach the stresses expected for Stokes flow around a buoyant inclusion rising toward a rigid boundary: stresses change sign toward the rigid boundary. Exactly opposite stresses occur at the bottom of the inclusion ($\phi=\pi$).

To test the effects of a free surface on viscoelastic stress relaxation, we solve a half-space viscoelastic chamber problem using stress functions (Fung, 1965), subject to overpressure boundary conditions. We use the bipolar coordinate system defined in terms of Cartesian coordinates by the complex mapping

$$x + iy = \frac{k(\sinh(\alpha) + i \sin(\beta))}{\cosh(\alpha) - \cos(\beta)} \quad (33)$$

where α and β are spatial coordinates, $i = \sqrt{-1}$, and k is a dimensional scaling factor that relates curves of constant α . For more details about this coordinate system and the method of stress functions, see e.g., (Jeffery, 1921; Karlstrom et al., 2009). We merely state the main results here. For this problem, boundary conditions are

$$\sigma_{\alpha\alpha}^{\text{in}}|_{\alpha=\alpha_1} = \Delta P \quad (34)$$

$$\sigma_{\alpha\alpha}^{\text{in}}|_{\alpha=\alpha_2} = \sigma_{\alpha\alpha}^{\text{out}}|_{\alpha=\alpha_2} \quad (35)$$

$$u_{\alpha}^{\text{in}}|_{\alpha=\alpha_2} = u_{\alpha}^{\text{out}}|_{\alpha=\alpha_2} \quad (36)$$

$$\sigma_{\alpha\beta}|_{\alpha=\alpha_0} = \sigma_{\alpha\alpha}|_{\alpha=0} = \sigma_{\alpha\beta}|_{\alpha=0} = 0, \quad (37)$$

where α_1 and α_2 are related to R_1 and R_2 in the polar coordinate system through

$$R_i = k \operatorname{csch}(\alpha_i) \quad (38)$$

for $i = 1, 2$.

Stress functions that satisfy the appropriate equilibrium equations and these boundary conditions take the form

$$\chi^{\text{in}}(\alpha, \beta) = \frac{k}{\cosh(\alpha) - \cos(\beta)} (A_1 \cosh(\alpha) + B_1 \sinh(\alpha) + C_1 \alpha (\cosh(\alpha) - \cos(\beta)) + (D_1 \cosh(2\alpha) + E_1 \sinh(2\alpha)) \cos(\beta)), \quad (39)$$

$$\chi^{\text{out}}(\alpha, \beta) = \frac{k}{\cosh(\alpha) - \cos(\beta)} (A_2 \cosh(\alpha) + B_2 \alpha (\cosh(\alpha) - \cos(\beta)) + (C_2 \cosh(2\alpha) + D_2 \sinh(2\alpha)) \cos(\beta)). \quad (40)$$

Stresses that correspond to these functions are

$$\sigma_{\alpha\alpha, \text{in}}(\alpha, \beta) = \frac{1}{k} (A_1 + C_1 (\cos(\beta) - \cosh(\alpha)) \sinh(\alpha) + \cosh(2\alpha) \times (D_1 - 2E_1 \cos(\beta) \sinh(\alpha)) + (E_1 - 2D_1 \cos(\beta) \sinh(\alpha)) \times \sinh(2\alpha)), \quad (41)$$

$$\sigma_{\beta\beta, \text{in}}(\alpha, \beta) = \frac{1}{k} (A_1 + 4D_1 \cos(\beta) \cosh^3(\alpha) - D_1 \cosh(2\alpha) + (C_1 - 2E_1) \times \cosh(\alpha) \sinh(\alpha) + \cos(\beta) (-C_1 + 4E_1 + 2E_1 \cosh(2\alpha)) \times \sinh(\alpha) + 2 \cos(2\beta) (D_1 \cosh(2\alpha) + E_1 \sinh(2\alpha))), \quad (42)$$

$$\sigma_{\alpha\beta, \text{in}}(\alpha, \beta) = \frac{1}{k} (\cos(\beta) - \cosh(\alpha)) \sin(\beta) (C_1 - 2E_1 \cosh(2\alpha) - 2D_1 \sinh(2\alpha)), \quad (43)$$

$$\sigma_{\alpha\alpha, \text{out}}(\alpha, \beta) = \frac{1}{k} (A_2 + B_2 (\cos(\beta) - \cosh(\alpha)) \sinh(\alpha) + \cosh(2\alpha) \times (C_2 - 2D_2 \cos(\beta) \sinh(\alpha)) + (D_2 - 2C_2 \cos(\beta) \sinh(\alpha)) \times \sinh(2\alpha)), \quad (44)$$

$$\sigma_{\beta\beta, \text{out}}(\alpha, \beta) = \frac{1}{k} (A_2 + 4C_2 \cos(\beta) \cosh^3(\alpha) - C_2 \cosh(2\alpha) + (B_2 - 2D_2) \times \cosh(\alpha) \sinh(\alpha) + \cos(\beta) (-B_2 + 4D_2 + 2D_2 \cosh(2\alpha)) \times \sinh(\alpha) - 2 \cos(2\beta) (C_2 \cosh(2\alpha) + D_2 \sinh(2\alpha))), \quad (45)$$

$$\sigma_{\alpha\beta, \text{out}}(\alpha, \beta) = \frac{1}{k} ((\cos(\beta) - \cosh(\alpha)) \sin(\beta) (B_2 - 2D_2 \cosh(2\alpha) - C_2 \sinh(2\alpha))), \quad (46)$$

and displacements outside the shell are

$$U_{\alpha, \text{out}}(\alpha, \beta) = (\cos(\beta) ((D_2(\lambda_2 - \mu_2) - 4B_2(\lambda_2 + \mu_2)) \cosh(\alpha) D_2(\lambda_2 + \mu_2) \times \cosh(3\alpha) + 2(C_2 \lambda_2 + A_2 \mu_2 + C_2(\lambda_2 + \mu_2) \cosh(2\alpha)) \times \sinh(\alpha) + (\lambda_2 + \mu_2)(2B_2 + (-2D_2 + B_2) \cosh(2\alpha) - 2C_2 \sinh(2\alpha)) + \cos(2\beta)(B_2(\lambda_2 + \mu_2) + 2D_2 \mu_2 \cosh(2\alpha) + 2C_2 \mu_2 \sinh(2\alpha))) / (4\mu_2(\lambda_2 + \mu_2)(\cos(\beta) - \cosh(\alpha)))$$

$$U_{\beta, \text{out}}(\alpha, \beta) = (\sin(\beta) ((\lambda_2 + 2\mu_2)(\cosh(2\alpha)(2C_2 \cos(\beta) + D_2 \sinh(\alpha)) + (2D_2 \cos(\beta) + C_2 \sinh(\alpha)) \sinh(2\alpha)) + \cosh(\alpha) \times (A_2 \mu_2 - (2\lambda_2 + 3\mu_2)(C_2 \cosh(2\alpha) + D_2 \sinh(2\alpha)))) \div (2\mu_2(\lambda_2 + \mu_2)(\cos(\beta) - \cosh(\alpha))). \quad (48)$$

The constants $A_1, B_1, C_1, D_1, E_1, A_2, B_2, C_2, D_2$, are evaluated to satisfy boundary conditions (34)–(37), and are

$$A_1 = (-2k\Delta P(-\operatorname{csch}(\alpha_1 - \alpha_2)(\lambda_1 + 2\mu_1)\mu_2(\lambda_2 + \mu_2) \sinh^2(\alpha_2) + \cosh(\alpha_1) \cosh(2\alpha_2)(\lambda_1 + \mu_1)(\cosh(2\alpha_2) \times (\mu_1 - \mu_2)(\lambda_2 + \mu_2) + \mu_2(\lambda_2 + \mu_1 + \mu_2)) \sinh(\alpha_2) - \cosh(\alpha_2)(\cosh(2\alpha_2) - 2) \sinh(\alpha_1)(\lambda_1 + \mu_1)(\cosh(2\alpha_2) \times (\mu_1 - \mu_2)(\lambda_2 + \mu_2) + \mu_2(\lambda_2 + \mu_1 + \mu_2)))) \div (\mu_1(2\mu_2((\sinh(\alpha_1 - 3\alpha_2) - 4 \sinh(\alpha_1 - \alpha_2) + \sinh(3\alpha_1 - \alpha_2)) \mu_1 \cosh^2(\alpha_2) + 4 \cosh^2(\alpha_1 - \alpha_2) \sinh^2(\alpha_2) \sinh(\alpha_1 + \alpha_2)\mu_2 + \lambda_2(8 \cosh^2(\alpha_1 - \alpha_2) \sinh(\alpha_1 + \alpha_2)\mu_2 \sinh^2(\alpha_2) + \cosh(2\alpha_2) \times (\sinh(\alpha_1 - 3\alpha_2) - 4 \sinh(\alpha_1 - \alpha_2) + \sinh(3\alpha_1 - \alpha_2))\mu_1)) + \lambda_1(2\mu_2((\sinh(\alpha_1 - 3\alpha_2) - 4 \sinh(\alpha_1 - \alpha_2) + \sinh(3\alpha_1 - \alpha_2))\mu_1 \times \cosh^2(\alpha_2) + \sinh^2(\alpha_2)(-\sinh(\alpha_1 - 3\alpha_2) + 2 \sinh(\alpha_1 - \alpha_2) + \sinh(\alpha_1 + \alpha_2))\mu_2) + \lambda_2(2(-\sinh(\alpha_1 - 3\alpha_2) + 2 \sinh(\alpha_1 - \alpha_2) + \sinh(\alpha_1 + \alpha_2))\mu_2 \sinh^2(\alpha_2) + \cosh(2\alpha_2) \times (\sinh(\alpha_1 - 3\alpha_2) - 4 \sinh(\alpha_1 - \alpha_2) + \sinh(3\alpha_1 - \alpha_2))\mu_1)))$$

$$B_1 = (k\Delta P \cosh(\alpha_1 - \alpha_2)(\lambda_1 + \mu_1)(4\lambda_1 \sinh^2(\alpha_2)\lambda_2(\mu_1 - \mu_2) - \mu_2(\mu_2 \sinh^2(\alpha_2) + \mu_1)) + \mu_1(4(\cosh(2\alpha_2) + 3)(\mu_1 - \mu_2)\mu_2 \times \sinh^2(\alpha_2) + \lambda_2((6 \cosh(2\alpha_2) + \cosh(4\alpha_2) - 3)\mu_1 - 4(\cosh(2\alpha_2) + 3) \sinh^2(\alpha_2)\mu_2))) / (\mu_1(\mu_1(2\mu_2((\sinh(\alpha_1 - 3\alpha_2) - 4 \sinh(\alpha_1 - \alpha_2) + \sinh(3\alpha_1 - \alpha_2))\mu_1 \cosh^2(\alpha_2) + 4 \cosh^2(\alpha_1 - \alpha_2) \sinh^2(\alpha_2) \sinh(\alpha_1 + \alpha_2)\mu_2 + \lambda_2(8 \cosh^2(\alpha_1 - \alpha_2) \times \sinh(\alpha_1 + \alpha_2)\mu_2 \sinh^2(\alpha_2) + \cosh(2\alpha_2)(\sinh(\alpha_1 - 3\alpha_2) - 4 \sinh(\alpha_1 - \alpha_2) + \sinh(3\alpha_1 - \alpha_2))\mu_1)) + \lambda_1(2\mu_2((\sinh(\alpha_1 - 3\alpha_2) - 4 \sinh(\alpha_1 - \alpha_2) + \sinh(3\alpha_1 - \alpha_2))\mu_1 \cosh^2(\alpha_2) + \sinh^2(\alpha_2)(-\sinh(\alpha_1 - 3\alpha_2) + 2 \sinh(\alpha_1 - \alpha_2) + \sinh(\alpha_1 + \alpha_2))\mu_2) + \lambda_2(2(-\sinh(\alpha_1 - 3\alpha_2) + 2 \sinh(\alpha_1 - \alpha_2) + \sinh(\alpha_1 + \alpha_2))\mu_2 \sinh^2(\alpha_2) + \cosh(2\alpha_2) \times (\sinh(\alpha_1 - 3\alpha_2) - 4 \sinh(\alpha_1 - \alpha_2) + \sinh(3\alpha_1 - \alpha_2))\mu_1)))$$

$$C_1 = (-4k\Delta P \cosh(\alpha_1 - \alpha_2)\mu_1((\lambda_1 - \lambda_2 + \mu_1 - \mu_2)\mu_2 + \cosh(2\alpha_2) \times (\lambda_2 + \mu_2)(\lambda_1 + \mu_1 + \mu_2))) / (\mu_1(2\mu_2((\sinh(\alpha_1 - 3\alpha_2) - 4 \sinh(\alpha_1 - \alpha_2) + \sinh(3\alpha_1 - \alpha_2))\mu_1 \cosh^2(\alpha_2) + 4 \cosh^2(\alpha_1 - \alpha_2) \sinh^2(\alpha_2) \sinh(\alpha_1 + \alpha_2)\mu_2 + \lambda_2(8 \cosh^2(\alpha_1 - \alpha_2) \times \sinh(\alpha_1 + \alpha_2)\mu_2 \sinh^2(\alpha_2) + \cosh(2\alpha_2)(\sinh(\alpha_1 - 3\alpha_2) - 4 \sinh(\alpha_1 - \alpha_2) + \sinh(3\alpha_1 - \alpha_2))\mu_1)) + \lambda_1(2\mu_2((\sinh(\alpha_1 - 3\alpha_2) - 4 \sinh(\alpha_1 - \alpha_2) + \sinh(3\alpha_1 - \alpha_2))\mu_1 \cosh^2(\alpha_2) + \sinh^2(\alpha_2)(-\sinh(\alpha_1 - 3\alpha_2) + 2 \sinh(\alpha_1 - \alpha_2) + \sinh(\alpha_1 + \alpha_2))\mu_2) + \lambda_2(2(-\sinh(\alpha_1 - 3\alpha_2) + 2 \sinh(\alpha_1 - \alpha_2) + \sinh(\alpha_1 + \alpha_2))\mu_2 \sinh^2(\alpha_2) + \cosh(2\alpha_2) \times (\sinh(\alpha_1 - 3\alpha_2) - 4 \sinh(\alpha_1 - \alpha_2) + \sinh(3\alpha_1 - \alpha_2))\mu_1)))$$

$$D_1 = (-k\Delta P \operatorname{csch}(\alpha_1 - \alpha_2)(\cosh(2\alpha_2)\mu_1((\lambda_1 - \lambda_2 + \mu_1 - \mu_2)\mu_2 + \cosh(2\alpha_2)(\lambda_2 + \mu_2)(\lambda_1 + \mu_1 + \mu_2)) + \cosh(2\alpha_1)(-\lambda_1 - \mu_1) \times (\cosh(2\alpha_2)(\mu_1 - \mu_2)(\lambda_2 + \mu_2) + \mu_2(\lambda_2 + \mu_1 + \mu_2))) \div (\mu_1(2\mu_2((\sinh(\alpha_1 - 3\alpha_2) - 4 \sinh(\alpha_1 - \alpha_2) + \sinh(3\alpha_1 - \alpha_2))\mu_1 \cosh^2(\alpha_2) + 4 \cosh^2(\alpha_1 - \alpha_2) \sinh^2(\alpha_2) \sinh(\alpha_1 + \alpha_2)\mu_2 + \lambda_2(8 \cosh^2(\alpha_1 - \alpha_2) \sinh(\alpha_1 + \alpha_2)\mu_2 \sinh^2(\alpha_2) + \cosh(2\alpha_2) \times (\sinh(\alpha_1 - 3\alpha_2) - 4 \sinh(\alpha_1 - \alpha_2) + \sinh(3\alpha_1 - \alpha_2))\mu_1)) + \lambda_1(2\mu_2((\sinh(\alpha_1 - 3\alpha_2) - 4 \sinh(\alpha_1 - \alpha_2) + \sinh(3\alpha_1 - \alpha_2))\mu_1 \times \cosh^2(\alpha_2) + \sinh^2(\alpha_2)(-\sinh(\alpha_1 - 3\alpha_2) + 2 \sinh(\alpha_1 - \alpha_2) + \sinh(\alpha_1 + \alpha_2))\mu_2) + \lambda_2(2(-\sinh(\alpha_1 - 3\alpha_2) + 2 \sinh(\alpha_1 - \alpha_2) + \sinh(\alpha_1 + \alpha_2))\mu_2 \sinh^2(\alpha_2) + \cosh(2\alpha_2) \times (\sinh(\alpha_1 - 3\alpha_2) - 4 \sinh(\alpha_1 - \alpha_2) + \sinh(3\alpha_1 - \alpha_2))\mu_1)))$$

$$E_1 = (k\Delta P \operatorname{csch}(\alpha_1 - \alpha_2)(2 \sinh(2\alpha_2)\mu_1(\lambda_1 - \lambda_2 + \mu_1 - \mu_2)\mu_2 - 2 \sinh(2\alpha_1)(\lambda_1 + \mu_1)(\lambda_2 + \mu_1 + \mu_2)\mu_2 - 2 \cosh(2\alpha_2) \times \sinh(2\alpha_1)(\lambda_1 + \mu_1)(\mu_1 - \mu_2)(\lambda_2 + \mu_2) + \sinh(4\alpha_2)\mu_1 \times (\lambda_2 + \mu_2)(\lambda_1 + \mu_1 + \mu_2))) / (2(\mu_1(2\mu_2((\sinh(\alpha_1 - 3\alpha_2) - 4 \sinh(\alpha_1 - \alpha_2) + \sinh(3\alpha_1 - \alpha_2))\mu_1 \cosh^2(\alpha_2) + 4 \cosh^2(\alpha_1 - \alpha_2) \sinh^2(\alpha_2) \sinh(\alpha_1 + \alpha_2)\mu_2 + \lambda_2(8 \cosh^2(\alpha_1 - \alpha_2) \times \sinh(\alpha_1 + \alpha_2)\mu_2 \sinh^2(\alpha_2) + \cosh(2\alpha_2)(\sinh(\alpha_1 - 3\alpha_2) - 4 \sinh(\alpha_1 - \alpha_2) + \sinh(3\alpha_1 - \alpha_2))\mu_1)) + \lambda_1(2\mu_2((\sinh(\alpha_1 - 3\alpha_2) - 4 \sinh(\alpha_1 - \alpha_2) + \sinh(3\alpha_1 - \alpha_2))\mu_1 \cosh^2(\alpha_2) + \sinh^2(\alpha_2)(-\sinh(\alpha_1 - 3\alpha_2) + 2 \sinh(\alpha_1 - \alpha_2) + \sinh(\alpha_1 + \alpha_2))\mu_2) + \lambda_2(2(-\sinh(\alpha_1 - 3\alpha_2) + 2 \sinh(\alpha_1 - \alpha_2) + \sinh(\alpha_1 + \alpha_2))\mu_2 \sinh^2(\alpha_2) + \cosh(2\alpha_2) \times (\sinh(\alpha_1 - 3\alpha_2) - 4 \sinh(\alpha_1 - \alpha_2) + \sinh(3\alpha_1 - \alpha_2))\mu_1)))$$

$$A_2 = -C_2 \tag{54}$$

$$B_2 = 2D_2 \tag{55}$$

$$C_2 = (2k\Delta P \cosh(\alpha_1 - \alpha_2) \sinh(2\alpha_2)(\lambda_1 + 2\mu_1)\mu_2(\lambda_2 + \mu_2)) \times (\mu_1(2\mu_2((\sinh(\alpha_1 - 3\alpha_2) - 4 \sinh(\alpha_1 - \alpha_2) + \sinh(3\alpha_1 - \alpha_2))\mu_1 \cosh^2(\alpha_2) + 4 \cosh^2(\alpha_1 - \alpha_2) \sinh^2(\alpha_2) \sinh(\alpha_1 + \alpha_2)\mu_2 + \lambda_2(8 \cosh^2(\alpha_1 - \alpha_2) \sinh(\alpha_1 + \alpha_2)\mu_2 \times \sinh^2(\alpha_2) + \cosh(2\alpha_2)(\sinh(\alpha_1 - 3\alpha_2) - 4 \sinh(\alpha_1 - \alpha_2) + \sinh(3\alpha_1 - \alpha_2))\mu_1)) + \lambda_1(2\mu_2((\sinh(\alpha_1 - 3\alpha_2) - 4 \sinh(\alpha_1 - \alpha_2) + \sinh(3\alpha_1 - \alpha_2))\mu_1 \cosh^2(\alpha_2) + \sinh^2(\alpha_2)(-\sinh(\alpha_1 - 3\alpha_2) + 2 \sinh(\alpha_1 - \alpha_2) + \sinh(\alpha_1 + \alpha_2))\mu_2) + \lambda_2(2(-\sinh(\alpha_1 - 3\alpha_2) + 2 \sinh(\alpha_1 - \alpha_2) + \sinh(\alpha_1 + \alpha_2))\mu_2 \times \sinh^2(\alpha_2) + \cosh(2\alpha_2) \times (\sinh(\alpha_1 - 3\alpha_2) - 4 \sinh(\alpha_1 - \alpha_2) + \sinh(3\alpha_1 - \alpha_2))\mu_1)))$$

$$\begin{aligned}
 D_2 = & (-2k\Delta P \cosh(\alpha_1 - \alpha_2) \cosh(2\alpha_2)(\lambda_1 + 2\mu_1)\mu_2(\lambda_2 + \mu_2)) \\
 & \div (\mu_1(2\mu_2((\sinh(\alpha_1 - 3\alpha_2) - 4 \sinh(\alpha_1 - \alpha_2) + \sinh(3\alpha_1 - \alpha_2))\mu_1 \\
 & \times \cosh^2(\alpha_2) + 4 \cosh^2(\alpha_1 - \alpha_2) \sinh^2(\alpha_2) \sinh(\alpha_1 + \alpha_2)\mu_2) \\
 & + \lambda_2(8 \cosh^2(\alpha_1 - \alpha_2) \sinh(\alpha_1 + \alpha_2)\mu_2 \sinh^2(\alpha_2) + \cosh(2\alpha_2) \\
 & \times (\sinh(\alpha_1 - 3\alpha_2) - 4 \sinh(\alpha_1 - \alpha_2) + \sinh(3\alpha_1 - \alpha_2))\mu_1)) \\
 & + \lambda_1(2\mu_2((\sinh(\alpha_1 - 3\alpha_2) - 4 \sinh(\alpha_1 - \alpha_2) + \sinh(3\alpha_1 - \alpha_2))\mu_1 \\
 & \times \cosh^2(\alpha_2) + \sinh^2(\alpha_2)(-\sinh(\alpha_1 - 3\alpha_2) + 2 \sinh(\alpha_1 - \alpha_2) \\
 & + \sinh(\alpha_1 + \alpha_2))\mu_2) + \lambda_2(2(-\sinh(\alpha_1 - 3\alpha_2) \\
 & + 2 \sinh(\alpha_1 - \alpha_2) + \sinh(\alpha_1 + \alpha_2))\mu_2 \sinh^2(\alpha_2) + \cosh(2\alpha_2) \\
 & \times (\sinh(\alpha_1 - 3\alpha_2) - 4 \sinh(\alpha_1 - \alpha_2) + \sinh(3\alpha_1 - \alpha_2))\mu_1)) \quad (57)
 \end{aligned}$$

The above expressions are then Laplace transformed using Eqs. (29)–(31), to obtain viscoelastic stresses and displacements.

The elastic stresses in this case differ significantly from the infinite space solutions in general, although they are asymptotically similar in the appropriate limiting conditions (Fig. 9). Deviatoric stresses around chambers at shallow depths are affected strongly by the free surface, and shell stresses exhibit an interesting change in topology as time progresses (Fig. 12). This change reflects the shear stresses induced on the chamber by the free surface, which gradually becomes dominant as isotropic deviatoric stresses relax away.

Appendix B. Thermal model

The melt fraction of a magma determines its rheological properties, and mixtures of magmas with different compositions are expected in chambers that grow through the discrete injection of basaltic dike

melt. We use one-parameter functions to relate melt fraction to temperature in our model. For amphibolite, we use the parameterization of Dufek and Bergantz (2005):

$$\begin{aligned}
 f(\mathbf{x}, t) = & -2.0968e^{-12}T^5 + 1.09308e^{-8}T^4 - 2.26718e^{-5}T^3 \\
 & + 2.33912e^{-2}T^2 - 12.0048T + 2451.69, \quad (58)
 \end{aligned}$$

where

$$T = T(\mathbf{x}, t) + 12(15 \text{ kbar} - P) \quad (59)$$

and we pick a pressure of $P = 10$ kbar to evaluate T . For tonalite, we use a parameterization drawn from (Petcovic and Dufek, 2005):

$$\begin{aligned}
 f(\mathbf{x}, t) = & 1.9852e^{-7}T^3(\mathbf{x}, t) - 4.8481e^{-4}T^2(\mathbf{x}, t) + 0.39547T(\mathbf{x}, t) \\
 & - 107.54 \quad (60)
 \end{aligned}$$

This parameterization fits the data of Piwinski and Wyllie (1968) well below melt fractions $f(\mathbf{x}, t) \sim 0.8$. Higher melt fractions, which are more poorly constrained by experiment, are parameterized by a linear segment with slope 0.18.

Basaltic melt fraction curves follow from the parameterizations in Dufek and Bergantz (2005), Petcovic and Dufek (2005) and the references therein. Anhydrous basalt follows the relation

$$\begin{aligned}
 f(\mathbf{x}, t) = & 2.79672e^{-11}T^4(\mathbf{x}, t) - 8.79939e^{-8}T^3(\mathbf{x}, t) \\
 & + 1.01622e^{-4}T^2(\mathbf{x}, t) - 5.02861e^{-2}T(\mathbf{x}, t) + 8.6693, \quad (61)
 \end{aligned}$$

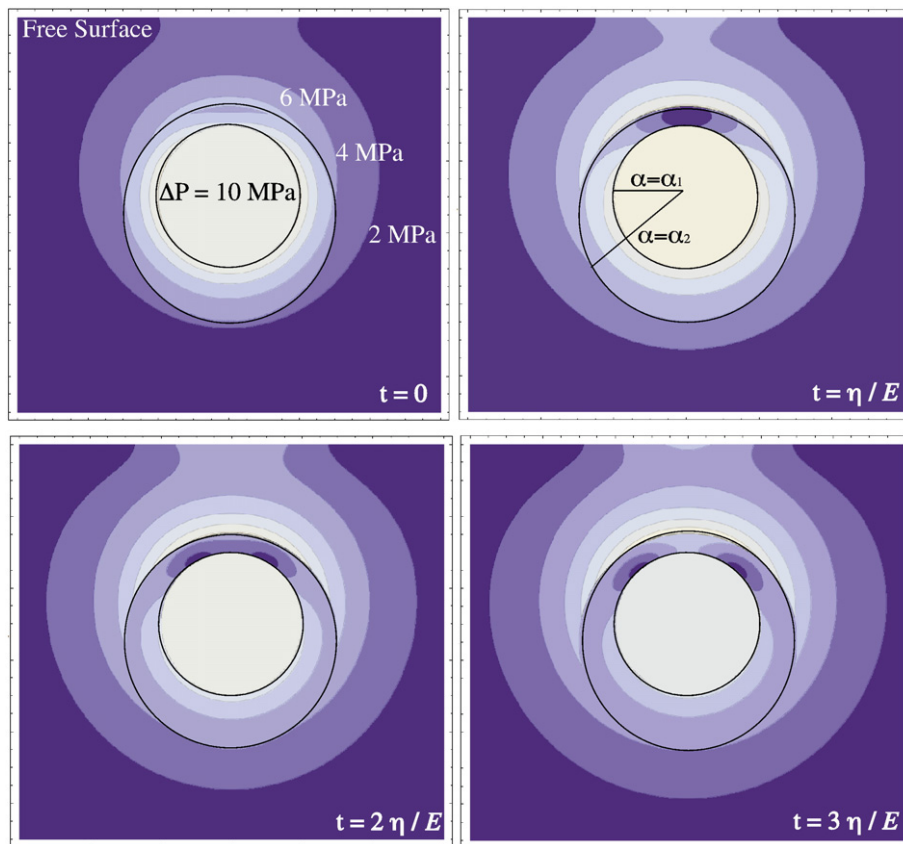


Fig. 12. Time evolution of greatest principle deviatoric stress field in the half-space solutions (Eqs. (41)–(46)). Chamber depth is 5 km, $R_1 = 2$ km, $R_2 = 3$ km (Eq. (38)), panel sizes are 12 km wide and 11 km high, with the stress free surface at the top. The up–down asymmetry in shell thickness is a feature of the bipolar coordinate system used to obtain the analytic solution, plotted here in Cartesian coordinates. Overpressure is set to 10 MPa, and stress contours are 2 MPa apart. Time between panels is multiples of the “Maxwell Time” η_{wr}/E , where η_{wr} is the shell viscosity, and E is Young’s Modulus. Note the topological change from one minima to two in the shell as deviatoric stresses are relaxed. This is a result of shear stresses induced on the chamber by the free surface.

whereas basalt with 2 wt.% H₂O has a melt fraction curve that accounts for the lower the solidus

$$f(\mathbf{x}, t) = 2.039e^{-9}T^3(\mathbf{x}, t) - 3.07e^{-6}T^2(\mathbf{x}, t) + 1.63e^{-3}T(\mathbf{x}, t) - 0.307. \quad (62)$$

Fig. 13 plots the four melt fraction curves used in this study, and the "critical melt fraction" of 0.6. As discussed in the Results section, it is the different forms of these curves (determined by the melting temperatures of modal mineral components) that account for the degree of crustal anatexis in our model runs.

The viscoelastic shell is defined on the basis of Eqs. (58)–(62), and the critical melt fraction of 0.6 that defines the transition from liquid-like to solid-like behavior. In calculating viscoelastic stresses, we use a constant viscosity throughout the shell, determined by the highest temperature material in the shell and an Arrhenius Law

$$\eta_{wr} = A \exp(Q / nRT) \quad (63)$$

where $A = \exp(15.4) \text{ MPa s}$, $Q = 515 \text{ kJ/mol}$, $n = 3.5$, and R is the molar gas constant. This viscosity law overpredicts shell viscosities, and it contains no model for crystal connectivity (e.g., Scaillet et al., 1998), but is nevertheless a commonly used formulation. The highest temperature in the shell results in a lower bound on shell viscosity in our model. Other choices (for example using the average temperature in shell) do affect details of the regime diagrams (Figs. 6 and 7), but the four dynamic regimes themselves are a robust result.

Inside the liquid region of the magma chamber, we use a linear mixing law to determine bulk material properties of the magma. Following Dufek and Bergantz (2005), we define a parameter $\gamma \in [0, 1]$ that defines the local volume fraction of intruded basalt or crustal melt. The mixture density is then defined by

$$\rho_{\text{mix}} = \gamma f_c \rho_c^l + \gamma(1-f_c)\rho_c^s + (1-\gamma)f_b \rho_b^l + (1-\gamma)(1-f_b)\rho_b^s, \quad (64)$$

mixture heat capacity by

$$c_{\text{mix}} = \gamma f_c c_c^l + \gamma(1-f_c)c_c^s + (1-\gamma)f_b c_b^l + (1-\gamma)(1-f_b)c_b^s, \quad (65)$$

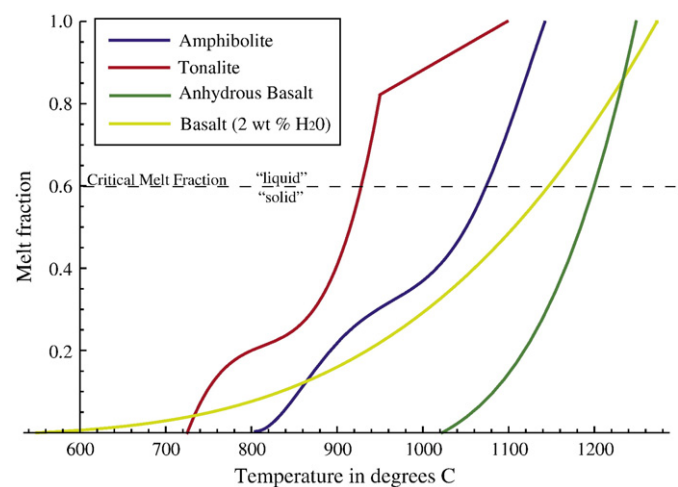


Fig. 13. Melt fraction vs. temperature curves used in this study. We use a piecewise continuous curve for tonalite that better represents melting of biotite at low melt fractions. Higher melt fractions are less well constrained experimentally, and hence do not warrant a more detailed fit. Note that these curves are parameterizations of melting experiments on "generic" but independent samples.

and mixture conductivity by

$$k_{\text{mix}} = \gamma f_c k_c^l + \gamma(1-f_c)k_c^s + (1-\gamma)f_b k_b^l + (1-\gamma)(1-f_b)k_b^s. \quad (66)$$

Here superscripts l and s refer to solid and liquid, while subscripts c and s stand for basalt and crust.

A number of factors in our model make keeping track of numerical errors important. The local nature of melting and solidification, along with the multiphase nature of the domain, create a spatially discontinuous and nonlinear heat conduction problem. We have performed tests to ensure that the predictor–corrector method used in our thermal calculation (Voller and Swaminathan, 1991) does in fact converge to the correct solution at each time step. Additional errors might occur during the discretization of melt into rings. Finite numerical resolution means that it is possible for small incoming melt flux to fall within grid resolution, so that the chamber does not conserve mass. This problem is overcome with sufficient spatial resolution.

References

Ague, J.J., Brimhall, G.H., 1988. Magmatic arc asymmetry and distribution of anomalous plutonic belts in the batholiths of California: effects of assimilation, crustal thickness, and depth of crystallization. *GSA Bulletin* 100, 912–927.

Albertz, M., 2005. Relationships between melt-induced rheological transitions and finite strain: observations from host rock pendants of the tuolumne intrusive suite, Sierra Nevada, California. *Journal of Structural Geology* 28, 1422–1444.

Annen, C., Sparks, R.S.J., 2002. Effects of repetitive emplacement of basaltic intrusions on thermal evolution and melt generation in the crust. *Earth and Planetary Science Letters* 203, 937–955.

Atkinson, B.K., Meredith, P.G., 1987. The theory of subcritical crack growth with application to minerals and rocks. In: Atkinson, B.K. (Ed.), *Fracture Mechanics of Rock*, Academic Press Geology Series. Academic Press, New York.

Bachmann, O., Bergantz, G.W., 2003. Rejuvenation of the fish canyon magma body: a window into the evolution of high-volume silicic magma systems. *Geology* 31 (9), 789–792.

Bachmann, O., Miller, C., de Silva, S., 2007. The volcanic–plutonic connection as a stage for understanding crustal magmatism. *Journal of Volcanology and Geothermal Research* 167, 1–23.

Barboza, S.A., Bergantz, G.W., 2000. Metamorphism and anatexis in the mafic complex contact aureole, Ivrea Zone, Northern Italy. *Journal of Petrology* 41 (8), 1307–1327.

Bonafede, M., Dragoni, M., Quarenì, F., 1986. Displacement and stress produced by a center of dilation and by a pressure source in a viscoelastic half-space: application to the study of ground deformation and seismicity at Campi Fleggeri, Italy. *Geophysical Journal of the Royal Astronomical Society* 87 (2), 455–485.

Bruce, P.M., Huppert, H.E., 1989. Thermal controls of basaltic fissure eruptions. *Nature* 342.

Canon-Tapia, E., Walker, G.P., 2004. Global aspects of volcanism: the perspectives of "plate tectonics" and "volcanic systems". *Earth Science Reviews* 66, 163–182.

Carrigan, C.R., 1988. Biot number and thermos bottle effect: implications for magma-chamber convection. *Geology* 16, 771–774.

Cawthorn, R.G., Walraven, F., 1998. Emplacement and crystallization time for the Bushveld Complex. *Journal of Petrology* 39 (9), 1669–1687.

Chen, Y.J., 1996. Constraints on melt production rate beneath the mid-ocean ridges based on passive flow models. *Pure and Applied Geophysics* 146 (3/4), 586–620.

Chen, Z., Jin, Z.-H., 2006. Magma-driven subcritical crack growth and implications for dike initiation from a magma chamber. *Geophysical Research Letters* 33, L19307. doi:10.1029/2006GL026979.

Christensen, N.I., Mooney, W., 1995. Seismic velocity structure and composition of the continental crust: a global view. *Journal of Geophysical Research* 100 (B7), 9761–9788.

Clemens, J.D., Mawer, C.K., 1992. Granitic magma transport by fracture propagation. *Tectonophysics* 204, 339–360.

Coleman, D.S., Gray, W., Glazner, A.F., 2004. Rethinking the emplacement and evolution of zoned plutons: geochronologic for incremental assembly of the tuolumne intrusive suite, California. *Geology* 32 (5), 433–436 May.

Cox, K.G., 1993. Continental magmatic underplating. *Philosophical Transaction of the Royal Society of London* 342, 155–16.

de Silva, S.L., Gosnold, W.D., 2007. Episodic construction of batholiths: insights from the spatiotemporal development of an ignimbrite flare-up. *Journal of Volcanology and Geothermal Research* 167, 320–335.

DePaolo, D.J., 1981. Trace element and isotopic effects of combined wallrock assimilation and fractional crystallization. *Earth and Planetary Science Letters* 53, 189–202.

Dimalanta, C., Taira, A., Yumul Jr., G.P., Tokuyama, H., Mochizuki, K., 2002. New rates of western Pacific island arc magmatism from seismic and gravity data. *Earth and Planetary Science Letters* 202, 105–115.

Dobran, F., 2001. *Volcanic Processes: Mechanisms in Material Transport*. Kluwer Academic/Plenum.

Dragoni, M., Magnaneni, C., 1989. Displacement and stress produced by a pressurized, spherical magma chamber, surrounded by a viscoelastic shell. *Physics of the Earth and Planetary Interiors* 56, 316–328.

- Dufek, J., Bergantz, G.W., 2005. Lower crustal magma genesis and preservation: a stochastic framework for the evaluation of basalt–crust interaction. *Journal of Petrology* 46 (11), 2167–2195.
- Dumond, G., Mahan, K.H., Williams, M.L., Karlstrom, K.E., 2007. Crustal segmentation, composite looping pressure–temperature paths, and magma-enhanced metamorphic field gradients: upper granite gorge, grand canyon, USA. *GSA Bulletin* 119 (1/2), 202–220 January/February.
- Ernst, R.E., Buchan, K.L., 1997. Layered mafic intrusions: a model for their feeder systems and relationship with giant dyke swarms and mantle plume centres. *South African Journal of Geology* 100 (4), 319–334.
- Ernst, R.E., Head, J.W., Parfitt, E., Grosfils, E.B., Wilson, L., 1995. Giant radiating dyke swarms on earth and venus. *Earth Science Reviews* 39.
- Farnetani, C.G., Richards, M.A., 1995. Thermal entrainment and melting in plumes. *Earth and Planetary Science Letters* 136, 251–267.
- Fowler, S.J., Spera, F.J., 2008. Phase equilibria trigger for explosive volcanic eruptions. *Geophysical Research Letters* 35 (L08309).
- Fung, Y.C., 1965. *Foundations of Solid Mechanics*. Prentice-Hall, Englewood Cliffs, N.J.
- Gaffney, E.S., Danjanac, B., Valentine, G.A., 2007. Localization of volcanic activity: 2. Effects of pre-existing structure. *Earth and Planetary Science Letters* 263, 323–338.
- Gerya, T.V., Yuen, D.A., Sevre, E.O.D., 2004. Dynamical causes for incipient magma chambers above slabs. *Geology* 32 (1), 89–92.
- Ghiorso, M.S., Carmichael, I.S.E., 1987. Modeling magmatic systems: petrologic applications. In: Carmichael, I.S.E., Eugster, H.P. (Eds.), *Thermodynamic modeling of geological materials: minerals, fluids and melts*. : Reviews in Mineralogy, volume 17. Mineralogical Society of America, Washington DC, pp. 467–499.
- Glazner, A.F., Coleman, D.S., Bartley, J.M., 2008. The tenuous connection between high-silica rhyolites and granodiorite plutons. *Geology* 36 (2), 183–186.
- Griffith, A.A., 1920. The phenomena of rupture and flow in solids. *Philosophical Transactions of the Royal Society of London* 221, 163–197.
- Grosfils, E.B., 2007. Magma reservoir failure on the terrestrial planets: assessing the importance of gravitational loading in simple elastic models. *Journal of Volcanology and Geothermal Research* 166, 47–75.
- Gudmundsson, A., 1988. Effect of tensile stress concentration around magma chambers on intrusion and extrusion frequencies. *Journal of Volcanology and Geothermal Research* 35, 179–194.
- Gudmundsson, A., 2006. How local stresses control magma-chamber ruptures, dyke injections, and eruptions in composite volcanoes. *Earth Science Reviews* 79, 1–31.
- Hanson, R.B., Glazner, A.F., 1995. Thermal requirements for extensional emplacements of granitoids. *Geology* 23 (3), 213–216.
- Harris, C., Pronost, J.J.M., Ashwal, L.D., Cawthorn, R.G., 2005. Oxygen and hydrogen isotope stratigraphy of the Rustenburg layered suite, Bushveld Complex: constraints on crustal contamination. *Journal of Petrology* 46 (3), 579–601.
- Hatton, C.J., 1995. Mantle plume origin for the Bushveld and Ventersdorp magmatic provinces. *Journal of African Earth Sciences* 21 (4), 571–577.
- Helz, R.T., 1982. Reviews in Mineralogy, volume 9B, chapter Phase relations and compositions of amphiboles produced in studies of the melting behavior of rocks. Mineralogical Society of America, Washington DC, pp. 279–347.
- Holtzman, B.K., Groebner, N.J., Zimmerman, M.E., Ginsber, S.B., Kohlstedt, D.L., 2003. Stress-driven melt segregation in partially molten rocks. *Geochemistry Geophysics Geosystems* 40 (5) May.
- Hort, M., 1997. Cooling and crystallization in sheet-like magma bodies revisited. *Journal of Volcanology and Geothermal Research* 76, 297–317.
- Hort, M., 1998. Abrupt change in magma liquidus temperature because of volatile loss or magma mixing: effects on nucleation, crystal growth and thermal history of the magma. *Journal of Petrology* 39 (5), 1063–1076.
- Huber, C., Bachmann, O., Manga, M., 2009. Homogenization processes in silicic magma chambers by stirring and mushification (latent heat buffering). *Earth and Planetary Science Letters* 283, 38–43.
- Hughes, G.R., Mahood, G.A., 2008. Tectonic controls on the nature of large silicic calderas in volcanic arcs. *Geology* 36 (8), 627–630.
- Hui, H., Zhang, Y., 2007. Toward a general viscosity equation for natural anhydrous and hydrous silicate melts. *Geochimica et Cosmochimica Acta* 71, 403–416.
- Huppert, H.E., Woods, A.W., 2002. The role of volatiles in magma chamber dynamics. *Nature* 420, 493–495.
- Ito, G., Martel, S.J., 2002. Focusing of magma in the upper mantle through dike interaction. *Journal of Geophysical Research* 107 (B10), 2223–2241.
- Jaeger, J.C., Cook, N.G.W., 1969. *Fundamentals of Rock Mechanics*. Methuen, London, volume 513 pp.
- Jagoutz, O., Muntener, O., Burg, J.-P., Ulmer, P., Jagoutz, E., 2006. Lower continental crust formation through focused flow in km-scale melt conduits: the zoned ultramafic bodies of the chilas complex in the kohistan island arc (NW Pakistan). *Earth and Planetary Science Letters* 242, 320–342.
- Jeffery, G.B., 1921. Plain stress and plane strain in bipolar co-ordinates. *Philosophical Transactions of the Royal Society of London A* 221, 265–293.
- Jellinek, A.M., DePaolo, D.J., 2003. A model for the origin of large silicic magma chambers: precursors of caldera-forming eruptions. *Bulletin of Volcanology* 65, 363–381.
- Johnson, T.E., Gibson, R.L., Brown, M., Buick, I.S., Cartwright, I., 2003. Partial melting of metapelitic rocks beneath the Bushveld Complex, South Africa. *Journal of Petrology* 44 (5), 789–813.
- Karlstrom, L., Dufek, J., Manga, M., 2009. Organization of volcanic plumbing through magmatic lensing by magma chambers and volcanic loads. *Journal of Geophysical Research* 114 (B10204). doi:10.1029/2009JB006339.
- Kavanagh, J.L., Menand, T., Sparks, R.S.J., 2006. An experimental investigation of sill formation and propagation in layered elastic media. *Earth and Planetary Science Letters* 245, 799–813.
- Kruger, F.J., 2005. Filling the Bushveld Complex magma chamber: lateral expansion, roof and floor interaction, magmatic unconformities, and the formation of giant chromitite, PGE and Ti-V-magnetite deposits. *Mineralium Deposita* 40, 451–472.
- Kühn, D., Dahm, T., 2008. Numerical modelling of dyke interaction and its influence on oceanic crust formation. *Tectonophysics* 447, 53–65.
- Lengline, O., Marsan, D., Got, J.-L., Pinel, V., Ferrazzini, V., Okubo, P.G., 2008. Seismicity and deformation induced by magma accumulation at three basaltic volcanoes. *Journal of Geophysical Research* 113 (B12305).
- Lipman, P.W., 2007. Incremental assembly and prolonged consolidation of cordilleran magma chambers: evidence from the southern rocky mountain volcanic field. *Geosphere* 3 (1), 42–70.
- Majer, W.D., Arndt, N.T., Curl, E.A., 2000. Progressive crustal contamination of the Bushveld Complex: evidence from nd isotopic analyses of the cumulate rocks. *Contributions to Mineralogy and Petrology* 140, 316–327.
- Manno, I., 1999. Introduction to the Monte-Carlo Method. Akademiai Kiado, Budapest.
- Marsh, B.D., 1981. On the crystallinity, probability of occurrence, and rheology of lava and magma. *Contributions to Mineralogy and Petrology* 78, 85–98.
- Marsh, B.D., 1989. On convective style and vigor in sheet-like magma chambers. *Journal of Petrology* 30 (3), 479–530.
- Matzel, J.E.P., Bowring, S.A., 2006. Time scales of pluton construction at differing crustal levels: examples from the mount Stuart and Tenpeak intrusions, North Cascades, Washington. *GSA Bulletin* 118 (11/12), 1412–1430.
- McNulty, B.A., Tong, W., Tobisch, O.T., 1996. Assembly of a dike-fed magma chamber: the jackass lakes pluton, central Sierra Nevada, California. *GSA Bulletin* 108 (8), 926–940.
- McTigue, D.F., 1987. Elastic stress and deformation near a finite spherical magma body—resolution of the point-source paradox. *Journal of Geophysical Research* 92 (B12), 12931–12940.
- Melnik, O., Sparks, R.S.J., 2005. Controls on magma flow dynamics during lava dome building eruptions. *Journal of Geophysical Research* 110 (B02209).
- Meriaux, Lister, 2002. Calculation of dike trajectories from volcanic centers. *Journal of Geophysical Research* 107 (B4), 2077–2087.
- Miller, J.S., Matzel, J.E.P., Miller, C.F., Burgess, S.D., Miller, R.B., 2007. Zircon growth and recycling during the assembly of large, composite arc plutons. *Journal of Volcanology and Geothermal Research* 167, 282–299.
- Miller, R.B., Paterson, S.R., 1999. In defense of magmatic diapirs. *Journal of Structural Geology* 21, 1161–1173.
- Muller, J.R., Ito, G., Martel, S.J., 2001. Effects of volcano loading on dike propagation in an elastic half-space. *Journal of Geophysical Research* 106 (B6), 11101–11113.
- Newman, A.V., Dixon, T.H., Ofoegbu, G.I., Dixon, J.E., 2001. Geodetic and seismic constraints on recent activity at Long Valley caldera, California: evidence for viscoelastic rheology. *Journal of Volcanology and Geothermal Research* 105, 183–206.
- Olson, P., 1994. *Magmatic Systems, chapter Mechanics of flood basalt magmatism*. Academic Press, New York, pp. 1–18.
- Paterson, S.R., Fowler, T.K., Miller, R.B., 1995. Pluton emplacement in arcs: a crustal-scale exchange process. *Transactions of the Royal Society of Edinburgh, Earth Sciences* 87, 115–123.
- Petcovic, H.L., Dufek, J., 2005. Modeling magma flow and cooling in dikes: implications for emplacement of Columbia river flood basalts. *Journal of Geophysical Research* 110 (B10201). doi:10.1029/2004JB003432.
- Petford, N., 1996. Dykes or diapirs? *Transactions of the Royal Society of Edinburgh, Earth Sciences* 87, 105–114.
- Pickett, D.A., Saleeby, L.B., 1993. Thermobarometric constraints on the depth of exposure and conditions of plutonism and metamorphism at deep levels of the sierra-nevada batholith, tehachapi mountains, california. *Journal of Geophysical Research-Solid Earth* 98 (B1), 609–629 January.
- Pinel, V., Jaupart, C., 2003. Magma chamber behavior beneath a volcanic edifice. *Journal of Geophysical Research* 108 (B2). doi:10.1029/2002JB001751.
- Pinel, V., Jaupart, C., 2005. Caldera formation by magma withdrawal from a reservoir beneath a volcanic edifice. *Earth and Planetary Science Letters* 230, 273–287.
- Piwinski, A.J., Wyllie, P.J., 1968. Experimental studies of igneous rock series; a zoned pluton in the Wallowa Batholith, Oregon. *Journal of Geology* 76, 483–499.
- Pollard, D.D., 1973. Derivation and evaluation of a mechanical model for sheet intrusions. *Tectonophysics* 19, 233–269.
- Roche, O., Druitt, T.H., 2001. Onset of caldera collapse during ignimbrite eruptions. *Earth and Planetary Science Letters* 191, 191–202.
- Roper, S.M., Lister, J.R., 2005. Buoyancy-driven crack propagation from an over-pressured source. *Journal of Fluid Mechanics* 536, 79–98.
- Rubin, A.M., 1995a. Getting granite dikes out of the source region. *Journal of Geophysical Research* B4, 5911–5929.
- Rubin, A.M., 1995. Propagation of magma-filled cracks. *Annual Reviews of Earth and Planetary Sciences* 23, 287–336.
- Rudnick, R.L., McDonough, W.E., O'Connell, R.J., 1998. Thermal structure, thickness and composition of continental lithosphere. *Chemical Geology* 145, 395–411.
- Ruprecht, P., Bergantz, G.W., Dufek, J., 2008. Modeling of gas-driven magmatic overturn: tracking of phenocryst dispersal and gathering during magma mixing. *Geochemistry Geophysics Geosystems* 9 (Q07017).
- Sartoris, G., Pozzi, J.P., Phillippe, C., Mouel, J.L.L., 1990. Mechanical stability of shallow magma chambers. *Journal of Geophysical Research* 95 (B4), 5141–5151.
- Scaillet, B., Holtz, F., Pichavant, M., 1998. Phase equilibrium constraints on the viscosity of silicic magmas; 1. volcanic–plutonic comparison. *Journal of Geophysical Research* 103 (B1), 27257–27266.
- Simon, J.L., Renne, P.R., Mundil, R., 2008. Implications of pre-eruptive magmatic histories of zircons for U–Pb geochronology of silicic extrusions. *Earth and Planetary Science Letters* 266, 182–194.
- Spera, F., 1980. Thermal evolution of plutons: a parameterized approach. *Science* 207 (4428), 299–301.

- Spera, F., Bohron, W.A., 2001. Energy-constrained open-system magmatic processes I: general model and energy-constrained assimilation and fractional crystallization (EC-AFC) formulation. *Journal of Petrology* 42 (5), 999–1018.
- Spiegelman, M., Kenyon, P., 1992. The requirements for chemical disequilibrium during magma migration. *Earth and Planetary Science Letters* 109, 611–620.
- Stevens, G., Gibson, R.L., Droop, G.T.R., 1997. Mid-crustal granulite facies metamorphism in the central Kaapvaal craton: the Bushveld Complex connection. *Precambrian Research* 82, 113–132.
- Tait, S., Jaupart, C., Vergnolle, S., 1989. Pressure, gas content and eruption periodicity of a shallow, crystallizing magma chamber. *Earth and Planetary Science Letters* 92, 107–123.
- Turner, J.S., Campbell, I.H., 1986. Convection and mixing in magma chambers. *Earth Science Reviews* 23, 255–352.
- Valentine, G.A., Krogh, K.E.C., 2006. Emplacement of shallow dikes and sills beneath a small basaltic volcano – the role of pre-existing structure (Paiute Ridge, Southern Nevada, USA). *Earth and Planetary Science Letters* 246 (3–4), 217–230.
- Voller, V.R., Swaminathan, C.R., 1991. General source-based method for solidification phase change. *Numerical Heat Transfer, Part B* 19, 175–189.
- Wallace, P.J., 2005. Volatiles in subduction zone magmas: concentrations and fluxes based on melt inclusion and volcanic gas data. *Journal of Volcanology and Geothermal Research* 140, 217–240.
- Williams, M.L., Karlstrom, K.E., Dumond, G., Mahan, K.H., 2009. Perspectives on the architecture of continental crust from integrated field studies of exposed isobaric sections. *Geological Society of America Special Paper* 456.
- Wolf, M.B., Wyllie, P.J., 1994. Dehydration-melting of amphibolite at 10 kbar: the effects of temperature and time. *Contributions to Mineralogy and Petrology* 115, 369–383.
- Yunker, L.W., Vogel, T.A., 1976. Plutonism and plate tectonics; the origin of circum-pacific batholiths. *Canadian Mineralogist* 14, 238–244.
- Yun, S., Segall, P., Zebker, H., 2006. Constraints on magma chamber geometry at Sierra Negra volcano, Galapagos Islands, based on INSAR observations. *Journal of Volcanology and Geothermal Research* 150, 232–243.
- Zak, J., Paterson, S.R., 2005. Characteristics of internal contacts in the Tuolumne batholith, Central Sierra Nevada, California (USA): implications for episodic emplacement and physical processes in a continental arc magma chamber. *GSA Bulletin* 117 (9/10), 1242–1255.